



THE UNIVERSITY *of* EDINBURGH

Edinburgh Research Explorer

The structural basis of rubisco phase separation in the pyrenoid

Citation for published version:

He, S, Chou, H-T, Matthies, D, Wunder, T, Meyer, MT, Atkinson, N, Martinez-Sanchez, A, Jeffrey, PD, Port, SA, Patena, W, He, G, Chen, VK, Hughson, FM, McCormick, AJ, Mueller-Cajar, O, Engel, BD, Yu, Z & Jonikas, MC 2020, 'The structural basis of rubisco phase separation in the pyrenoid', *Nature Plants*.
<https://doi.org/10.1038/s41477-020-00811-y>

Digital Object Identifier (DOI):

[10.1038/s41477-020-00811-y](https://doi.org/10.1038/s41477-020-00811-y)

Link:

[Link to publication record in Edinburgh Research Explorer](#)

Document Version:

Peer reviewed version

Published In:

Nature Plants

General rights

Copyright for the publications made accessible via the Edinburgh Research Explorer is retained by the author(s) and / or other copyright owners and it is a condition of accessing these publications that users recognise and abide by the legal requirements associated with these rights.

Take down policy

The University of Edinburgh has made every reasonable effort to ensure that Edinburgh Research Explorer content complies with UK legislation. If you believe that the public display of this file breaches copyright please contact openaccess@ed.ac.uk providing details, and we will remove access to the work immediately and investigate your claim.



14

15

16 **The Structural Basis of Rubisco Phase Separation in the Pyrenoid**

17

18 Shan He¹, Hui-Ting Chou^{2,10}, Doreen Matthies², Tobias Wunder³, Moritz T. Meyer¹, Nicky
19 Atkinson⁴, Antonio Martinez-Sanchez^{5,6}, Philip D. Jeffrey¹, Sarah A. Port¹, Weronika Patena¹,
20 Guanhua He¹, Vivian K. Chen⁷, Frederick M. Hughson¹, Alistair J. McCormick⁴, Oliver
21 Mueller-Cajar³, Benjamin D. Engel^{5,8,9}, Zhiheng Yu², Martin C. Jonikas^{1,*}

22

23 ¹Department of Molecular Biology, Princeton University, Princeton, NJ 08544, USA. ²Janelia
24 Research Campus, Howard Hughes Medical Institute, 19700 Helix Drive, Ashburn, VA 20147,
25 USA. ³School of Biological Sciences, Nanyang Technological University, 60 Nanyang Drive,
26 Singapore 637551, Singapore. ⁴SynthSys & Institute of Molecular Plant Sciences, School of
27 Biological Sciences, University of Edinburgh, Edinburgh, EH9 3BF, UK. ⁵Department of
28 Molecular Structural Biology, Max Planck Institute of Biochemistry, 82152 Martinsried,
29 Germany. ⁶Institute of Neuropathology, University of Göttingen Medical Center, 37075
30 Göttingen, Germany. ⁷Department of Biology, Stanford University, Stanford, CA 94305, USA.
31 ⁸Helmholtz Pioneer Campus, Helmholtz Zentrum München, 85764 Neuherberg, Germany.
32 ⁹Department of Chemistry, Technical University of Munich, Lichtenbergstraße 4, 85748
33 Garching, Germany. ¹⁰Present address: Department of Therapeutic Discovery, Amgen Discovery
34 Research, Amgen Inc., South San Francisco, CA 94080, USA.

35 *Correspondence and Lead Contact: mjonikas@princeton.edu.

36

37 **Abstract**

38 Approximately one-third of global CO₂ fixation occurs in a phase-separated algal organelle
39 called the pyrenoid. Existing data suggest that the pyrenoid forms by the phase separation of the
40 CO₂-fixing enzyme Rubisco with a linker protein; however, the molecular interactions
41 underlying this phase separation remain unknown. Here we present the structural basis of the
42 interactions between Rubisco and its intrinsically disordered linker protein EPYC1 (Essential
43 Pyrenoid Component 1) in the model alga *Chlamydomonas reinhardtii*. We find that EPYC1
44 consists of five evenly-spaced Rubisco-binding regions that share sequence similarity. Single-
45 particle cryo-electron microscopy of one of these regions in complex with Rubisco indicates that
46 each Rubisco holoenzyme has eight binding sites for EPYC1, one on each Rubisco small
47 subunit. Interface mutations disrupt binding, phase separation, and pyrenoid formation. Cryo-
48 electron tomography supports a model where EPYC1 and Rubisco form a co-dependent
49 multivalent network of specific low-affinity bonds, giving the matrix liquid-like properties. Our
50 results advance the structural and functional understanding of the phase separation underlying
51 the pyrenoid, an organelle that plays a fundamental role in the global carbon cycle.

52 Main Text

53 The CO₂-fixing enzyme Rubisco drives the global carbon cycle, mediating the
54 assimilation of approximately 100 gigatons of carbon per year¹. The gradual decrease of
55 atmospheric CO₂ over billions of years² has made Rubisco's job increasingly difficult, to the
56 point where CO₂ assimilation limits the growth rate of many photosynthetic organisms³. This
57 selective pressure is thought to have led to the evolution of CO₂ concentrating mechanisms,
58 which feed concentrated CO₂ to Rubisco to enhance growth⁴. Of these mechanisms, the most
59 poorly understood relies on the pyrenoid, a phase separated organelle⁵ found in the chloroplast of
60 nearly all eukaryotic algae and some land plants (Fig. 1a, b)^{6,7}. The pyrenoid enhances the
61 activity of Rubisco by clustering it around modified thylakoid membranes that supply Rubisco
62 with concentrated CO₂^{8,9}.

63 For decades, the mechanism for packaging the Rubisco holoenzyme into the pyrenoid
64 remained unknown. Recent work showed that in the leading model alga *Chlamydomonas*
65 *reinhardtii* (*Chlamydomonas* hereafter), the clustering of Rubisco into the pyrenoid matrix
66 requires the Rubisco-binding protein EPYC1¹⁰. EPYC1 and Rubisco are the most abundant
67 components of the pyrenoid and bind to each other. Moreover, combining purified EPYC1 and
68 Rubisco together produces phase-separated condensates¹¹ that mix internally at a rate similar to
69 that observed for the matrix *in vivo*⁵, suggesting that these two proteins are sufficient to form the
70 structure of the pyrenoid matrix. The sequence repeats within EPYC1 and eight-fold symmetry
71 of the Rubisco holoenzyme led us to hypothesize that EPYC1 and Rubisco each have multiple
72 binding sites for the other, allowing the two proteins to form a co-dependent condensate (Fig.
73 1c)¹⁰.

74 Here, we determined the structural basis that underlies the EPYC1-Rubisco condensate.
75 Using biophysical approaches, we found that EPYC1 has five evenly spaced Rubisco-binding
76 regions that share sequence homology and can bind to Rubisco as short peptides. We obtained
77 cryo-electron microscopy structures showing that each of EPYC1's Rubisco-binding regions
78 forms an α -helix that binds one of Rubisco's eight small subunits via salt bridges and
79 hydrophobic interactions. Mapping of these binding sites onto Rubisco holoenzymes within the
80 native pyrenoid matrix indicates that the linker sequences between Rubisco-binding regions on
81 EPYC1 are sufficiently long to connect together adjacent Rubisco holoenzymes. These

82 discoveries advance the understanding of the pyrenoid and provide a high-resolution structural
83 view of a phase-separated organelle.

84

85 **Results**

86

87 We could not directly determine the structure of full-length EPYC1 bound to Rubisco because
88 mixing the two proteins together produces phase-separated condensates¹¹. We thus aimed to first
89 identify Rubisco-binding regions on EPYC1, and subsequently to use a structural approach to
90 determine how these regions bind to Rubisco.

91

92 **EPYC1 has five nearly identical Rubisco-binding regions**

93 The intrinsically disordered nature of purified EPYC1¹¹ led us to hypothesize that the
94 Rubisco-binding regions of EPYC1 were short and could bind to Rubisco as peptides without a
95 need for tertiary folds. Therefore, to identify EPYC1 regions that bind to Rubisco, we
96 synthesized a peptide array consisting of 18 amino acid peptides tiling across the full length
97 EPYC1 sequence (Fig. 1d), and probed this array with native Rubisco purified from
98 *Chlamydomonas* cells (Fig. 1e, f).

99 Our tiling array revealed five evenly-spaced Rubisco-binding regions on EPYC1, each
100 consisting of a predicted α -helix and an upstream region (Fig. 1g, h and Supplementary Table 3).
101 We confirmed the binding regions using surface plasmon resonance (SPR; Extended Data Fig.
102 1b, c). Sequence alignment guided by the five binding regions revealed that mature EPYC1
103 consists entirely of five sequence repeats (Fig. 1i), in contrast to the previously defined four
104 repeats and two termini¹⁰ (Extended Data Fig. 1a). Our alignment indicates that the previously
105 defined EPYC1 N- and C- termini, which at the time were not considered part of the repeats,
106 actually share sequence homology with the central repeats.

107 The presence of a Rubisco-binding region on each of the previously defined EPYC1
108 repeats (Extended Data Fig. 1a) explains our yeast two-hybrid observations¹² that a single
109 EPYC1 repeat can interact with Rubisco, that knocking out the α -helix in an EPYC1 repeat
110 disrupts this interaction, and that decreasing the number of EPYC1 repeats leads to a
111 proportional decrease in EPYC1 interaction with Rubisco. It also explains our observations that

112 decreasing the number of EPYC1 repeats leads to a proportional decrease in the tendency of
113 EPYC1 and Rubisco to phase separate together¹¹.

114

115 **EPYC1 binds to Rubisco small subunits**

116 The sequence homology of the five Rubisco-binding regions suggests that each region binds to
117 Rubisco in a similar manner. To identify the binding site of EPYC1 on Rubisco, we determined
118 three structures by using single-particle cryo-electron microscopy. The first structure consists of
119 Rubisco in complex with peptide EPYC1₄₉₋₇₂, representing the first Rubisco-binding region of
120 EPYC1 (2.13 Å overall resolution; ~2.5 Å EPYC1 peptide local resolution; Fig. 2, Extended
121 Data Fig. 2-5; Supplementary Table 1). The second structure consists of Rubisco in complex
122 with a second peptide, EPYC1₁₀₆₋₁₃₅, representing the second, third and fourth Rubisco-binding
123 regions of EPYC1 (2.06 Å overall resolution, ~2.5 Å EPYC1 peptide local resolution, Extended
124 Data Fig. 6). The affinities of these peptides to Rubisco were low by protein interaction
125 standards ($K_D \sim 3$ mM; Extended Data Fig. 1d, e); thus, millimolar concentrations of peptide
126 were required to approach full occupancy of peptide bound to Rubisco. For reference purposes,
127 we also obtained a third structure of Rubisco in the absence of EPYC1 peptide (2.68 Å;
128 Extended Data Fig. 2 and 3), which was nearly identical to the previously published X-ray
129 crystallography structure¹³, with minor differences likely due to the absence of the substrate
130 analog 2-CABP in the active site of Rubisco in our sample¹⁴ (Extended Data Fig. 4).

131 The structures of Rubisco in complex with EPYC1₄₉₋₇₂ and of Rubisco in complex with
132 EPYC1₁₀₆₋₁₃₅ were remarkably similar, indicating that these two peptides and the corresponding
133 four regions of EPYC1 each bind to the same site on the Rubisco holoenzyme. The Rubisco
134 holoenzyme consists of a core of eight catalytic large subunits in complex with eight small
135 subunits, four of which cap each end of the holoenzyme (Fig. 2b-e). In each structure, an EPYC1
136 peptide was clearly visible bound to each Rubisco small subunit, suggesting that each Rubisco
137 holoenzyme can bind up to eight EPYC1s (Fig. 2b-e and Extended Data Fig. 6b, c).

138

139 **Salt bridges and a hydrophobic interface mediate binding**

140 Both the EPYC1₄₉₋₇₂ and EPYC1₁₀₆₋₁₃₅ peptides formed an extended chain that sits on top of the
141 Rubisco small subunit's two α -helices (Fig. 3a, b, Extended Data Fig. 6d, e). This binding site
142 explains our previous observations that mutations in the Rubisco small subunit α -helices

143 disrupted yeast two-hybrid interactions between EPYC1 and the Rubisco small subunit¹² and
144 prevented Rubisco's assembly into a pyrenoid *in vivo*¹⁵. The C-terminal regions of the EPYC1₄₉₋
145 ₇₂ and EPYC1₁₀₆₋₁₃₅ peptides (NW[R/K]QELESLR[N/S]) are well-resolved; each forms an α -
146 helix that runs parallel to helix B of the Rubisco small subunit (Fig. 3a, b). The peptides' N-
147 termini extend the trajectory of the helix and follow the surface of the Rubisco small subunit
148 (Fig. 2b-e, 3a-b and Extended Data Fig. 5, Extended Data Fig. 6b, c). The side chains of the
149 peptides' N-termini could not be well resolved, suggesting that these regions are more
150 conformationally flexible.

151 Our atomic models based on the density maps suggest that binding is mediated by salt
152 bridges and a hydrophobic interface. Three residue pairs of EPYC1₄₉₋₇₂ likely form salt bridges
153 (Fig. 3c, d and g): EPYC1 residues R64 and R71 interact with E24 and D23, respectively, of
154 Rubisco small subunit α -helix A, and EPYC1 residue E66 interacts with R91 of Rubisco small
155 subunit α -helix B. Furthermore, a hydrophobic interface is formed by W63, L67 and L70 of
156 EPYC1 and M87, L90 and V94 of Rubisco small subunit helix B (Fig. 3e-g). Similar interactions
157 were observed for the corresponding residues in EPYC1₁₀₆₋₁₃₅ (Extended Data Fig. 6f-j).

158

159 **Binding and phase separation require interface residues**

160 To determine the importance of individual EPYC1 residues for binding, we investigated the
161 impact on Rubisco binding of every possible single amino acid substitution for EPYC1's first
162 Rubisco-binding region by using a peptide array (Fig. 4a and Supplementary Table 4) and SPR
163 (Extended Data Fig. 7). Consistent with our structural model, the peptide array indicated that
164 EPYC1 salt bridge-forming residues R64, R71 and E66 and the hydrophobic interface residues
165 W63, L67 and L70 were all required for normal EPYC1 binding to Rubisco. The strong
166 agreement of our mutational analysis suggests that our structural model correctly represents
167 EPYC1's Rubisco-binding interface.

168 To determine the importance of EPYC1's Rubisco-binding regions for pyrenoid matrix
169 formation, we assayed the impact of mutations in these regions on formation of phase separated
170 droplets by EPYC1 and Rubisco *in vitro*. The phase boundary was shifted by mutating R64 in
171 the first Rubisco-binding region and the corresponding K or R in the other four Rubisco-binding
172 regions of EPYC1 (Fig. 4b and Extended Data Fig. 8), suggesting that the Rubisco-binding
173 regions mediate condensate formation.

174

175 **Pyrenoid matrix formation requires interface residues**

176 We validated the importance of Rubisco residues for binding to EPYC1 by yeast two-hybrid
177 assays (Fig. 5a and Extended Data Fig. 9). A Rubisco small subunit D23A mutation, which
178 eliminates the charge of the aspartate residue, had a severe impact on Rubisco small subunit
179 interaction with EPYC1, as expected from the contribution of that residue to a salt bridge with
180 R71 and homologous residues of EPYC1's Rubisco-binding regions. Likewise, E24A and R91A
181 each showed a moderate defect, consistent with the contributions of those residues to salt bridges
182 with R64 and E66 (and homologous residues) of EPYC1, respectively. Additionally, M87D and
183 V94D, mutations which convert hydrophobic residues to bulky charged residues, each had a
184 severe impact on interaction, as expected from the participation of those residues in the
185 hydrophobic interface. Combinations of these mutations abolished the interactions completely
186 (Extended Data Fig. 9).

187 To evaluate the importance of the binding interface *in vivo*, we generated
188 Chlamydomonas strains with point mutations in the binding interface. Rubisco small subunit
189 mutations D23A/E24A or M87D/V94D caused a growth defect under conditions requiring a
190 functional pyrenoid (Fig. 5b, Extended Data Fig. 10a-b). Furthermore, the mutants lacked a
191 visible pyrenoid matrix (Fig. 5c, d and Extended Data Fig. 10c), indicating that those Rubisco
192 small subunit residues are required for matrix formation *in vivo*. The Rubisco mutants retained
193 pyrenoid tubules¹⁶, as previously observed in other matrix-deficient mutants^{10,17-19}.

194 Together, our data demonstrate that EPYC1's Rubisco-binding regions bind to the
195 Rubisco small subunit α -helices via salt-bridge interactions and a hydrophobic interface,
196 enabling the condensation of Rubisco into the phase separated matrix.

197

198 **A structural model for pyrenoid matrix formation**

199 The presence of multiple Rubisco-binding regions along the EPYC1 sequence supports a model
200 where consecutive Rubisco-binding regions on the same EPYC1 polypeptide can bind to
201 different Rubisco holoenzymes and thus hold them together to form the pyrenoid matrix. If this
202 model is correct, we would expect that the ~40 amino acid "linker" regions between consecutive
203 Rubisco-binding regions on EPYC1 (Fig. 1g, i) would be sufficient to span the distance between
204 EPYC1-binding sites on neighboring Rubisco holoenzymes in the pyrenoid matrix. To test this

205 aspect of the model, we combined our atomic structure of the EPYC1-Rubisco interaction with
206 the precise positions and orientations of Rubisco holoenzymes within the pyrenoid matrix of
207 native cells that we had previously obtained by *in-situ* cryo-electron tomography⁵ (Fig. 6a, b).
208 We mapped the positions of EPYC1 binding sites onto Rubisco holoenzymes in the matrix and
209 measured the distances between nearest neighbor EPYC1 binding sites on adjacent holoenzymes
210 (Fig. 6c, binding sites on the same holoenzyme were excluded in this analysis). The observed
211 distances ranged from ~2 nm to ~7 nm, with a median distance of ~4 nm (Fig. 6d and
212 Supplementary Table 5).

213 A “linker” region of 40 amino acids is unlikely to be stretched to its maximum possible
214 length of 14 nm *in vivo* due to the high entropic cost of this configuration. To determine whether
215 a linker region can span the observed distances between nearest neighbor binding sites on
216 adjacent Rubisco holoenzymes, we used a simple physics model to calculate the energy required
217 to stretch a 40 amino acid chain to any given distance (Fig. 6d; see Methods). The model
218 indicates that stretching the chain to ~7 nm requires an energy of $3 k_B T$ (where k_B is the
219 Boltzmann constant and T is the temperature), which could reasonably be derived from thermal
220 fluctuations. Thus, our data suggest that the linker region between consecutive Rubisco-binding
221 sites on the EPYC1 polypeptide can span the distance between adjacent Rubisco holoenzymes to
222 hold the pyrenoid matrix together *in vivo*. It also appears likely that, in addition to bridging
223 neighboring Rubisco holoenzymes, consecutive Rubisco-binding regions on a given EPYC1 can
224 bind multiple sites on one Rubisco holoenzyme, as the distance between the nearest binding sites
225 on the same holoenzyme is < 9 nm.

226

227 **Discussion**

228

229 In this study, we have determined the structural basis for pyrenoid matrix formation for the first
230 time in any species. We found that in the model alga *Chlamydomonas*, the intrinsically
231 disordered protein EPYC1 has five regions of similar sequence that can bind to Rubisco as short
232 peptides. These EPYC1 regions form an α -helix that binds to the Rubisco small subunit α -helices
233 via salt bridges and hydrophobic interactions. EPYC1’s Rubisco-binding regions are spaced by
234 linker sequences that are sufficiently long to span the distance between binding sites on adjacent

235 Rubisco holoenzymes within the pyrenoid, allowing EPYC1 to serve as a molecular glue that
236 clusters Rubisco together to form the pyrenoid matrix (Fig. 6e).

237 The multivalency of EPYC1 and the high K_D (~ 3 mM; Extended Data Fig. 1e) of
238 individual Rubisco-binding regions are consistent with the emerging principle that cellular phase
239 separation is mediated by weak multivalent interactions²⁰. The high dissociation rate constant
240 ($>1/s$; Extended Data Fig. 1d) of individual Rubisco-binding regions explains how the pyrenoid
241 matrix can mix internally on the time scale of seconds⁵ despite the multivalency of EPYC1. The
242 even spacing of the five Rubisco-binding regions across EPYC1 is noteworthy and may be an
243 indication of selective pressure for an optimal distance between binding regions, and thus of an
244 optimal spacing between Rubisco holoenzymes in the matrix.

245 Knowledge of the EPYC1-Rubisco binding mechanism now opens doors to the molecular
246 characterization of the regulation of this interaction, which may govern the dissolution and
247 condensation of the matrix during cell division⁵ and in response to environmental factors²¹. For
248 example, phosphorylation of EPYC1²² may provide a mechanism to rapidly change the binding
249 affinity of EPYC1 to Rubisco. Inactivation of one Rubisco-binding region on EPYC1 would
250 yield four binding regions, which would allow two such EPYC1 molecules (each containing four
251 Rubisco-binding regions, for a total of eight Rubisco-binding regions) to form a mutually
252 satisfied complex with each Rubisco holoenzyme (containing eight EPYC1-binding sites), a
253 configuration that is predicted to favor dissolution of the matrix⁵.

254

255 **Our structures explain how other proteins bind to Rubisco**

256 In a parallel study (Meyer et al., please see unpublished manuscript provided as reference
257 material), we recently discovered that a common sequence motif is present on many pyrenoid-
258 localized proteins. The motif binds Rubisco, enabling recruitment of motif-containing proteins to
259 the pyrenoid and mediating adhesion between the matrix, pyrenoid tubules, and starch sheath.
260 This motif, [D/N]W[R/K]XX[L/I/V/A], is present in EPYC1's Rubisco-binding regions as
261 defined in the present study, and the motif residues mediate key binding interactions with
262 Rubisco. In our structures, the R/K of the motif is represented by R64 and K127 of EPYC1, each
263 of which forms a salt bridge with E24 of the Rubisco small subunit. The XX of the motif almost
264 always includes a D or E; in our structures this feature is represented by E66 and E129 of
265 EPYC1, each of which forms a salt bridge with R91 of the Rubisco small subunit. Finally, the W

266 and [L/I/V/A] of the motif are represented by W63/W126 and L67/L130 of EPYC1, which
267 contribute to the hydrophobic interactions with M87, L90 and V94 of the Rubisco small subunit.
268 The key roles of the motif residues in the interface presented here strongly suggest that the
269 structures we have obtained for motifs from EPYC1 also explain where and how all other
270 variants of the motif, including those found on the key pyrenoid proteins SAGA1, SAGA2,
271 RBMP1, RBMP2 and CSP41A, bind to Rubisco. Our observation that the Rubisco small subunit
272 D23A/E24A and M87D/V94D mutants exhibit a more severe disruption of the pyrenoid than the
273 *epyc1* mutant¹⁰ supports the idea that this region of Rubisco interacts not only with EPYC1, but
274 also with other proteins required for pyrenoid biogenesis, making this binding interaction a
275 central hub of pyrenoid biogenesis.

276

277 **Structural differences between the pyrenoid and carboxysomes**

278 Although α - and β -carboxysomes are morphologically, functionally and evolutionarily distinct
279 from the pyrenoid, their Rubisco is also thought to be clustered by linker proteins. Like EPYC1,
280 the α -carboxysome linker protein CsoS2²³ is intrinsically disordered and is proposed to bind
281 Rubisco as an unfolded peptide²⁴. In contrast, the β -carboxysome linker protein CcmM has been
282 proposed to bind Rubisco using folded globular domains^{25,26}. The use of an unfolded peptide as
283 in the case of EPYC1 and CsoS2 may provide the benefit of requiring fewer amino acids for
284 achieving the desired binding function. A notable difference is the location of the binding site on
285 Rubisco: whereas both carboxysomal linker proteins bind to the interface between two Rubisco
286 large subunits^{24,26}, EPYC1 binds to the Rubisco small subunit. It remains to be seen whether this
287 difference in binding site has functional consequences, such as impacts on the three-dimensional
288 packing of Rubisco.

289

290 **Our findings advance the ability to engineer a pyrenoid**

291 There is currently significant interest in engineering Rubisco condensates into
292 monocotyledonous crops such as wheat and rice to enhance yields²⁷⁻³⁰. Binding of EPYC1 to the
293 Rubisco small subunit presents a promising route for engineering a Rubisco condensate, as the
294 Rubisco small subunit is encoded in the nuclear genome, making it more easily amenable to
295 genetic modification in those crops than the chloroplast-encoded Rubisco large subunit³¹.
296 Knowledge of the binding mechanism now allows engineering of minimal sequence changes into

297 native crop Rubiscos to enable binding to EPYC1 and to other key proteins required to
298 reconstitute a functional pyrenoid.

299

300 **Insights into pyrenoid matrix formation in other species**

301 Pyrenoids appear to have evolved independently in different lineages through convergent
302 evolution^{7,32}. EPYC1, its Rubisco-binding sequences, and the amino acid residues that form the
303 EPYC1 binding site on the surface of Rubisco are conserved across the order Volvocales, as
304 evidenced from the genome sequences of *Tetrabaena socialis*, *Gonium pectorale* and *Volvox*
305 *carteri* (Supplementary Table 2). While the molecular mechanisms of matrix formation in other
306 lineages remain to be uncovered, candidate linker proteins have been identified based on
307 similarity of sequence properties to EPYC1¹⁰. We hypothesize that the matrix in other lineages is
308 formed based on similar principles to those we observed in *Chlamydomonas*. Our experimental
309 approach for characterizing the binding interaction provides a roadmap for future structural
310 studies of pyrenoids across the tree of life.

311

312 **We provide a structural view of a phase-separated organelle**

313 The pyrenoid matrix presents an unusual opportunity to study a two-component molecular
314 condensate where one of the components, Rubisco, is large and rigid, and the other component,
315 EPYC1, is a simple intrinsically disordered protein consisting of nearly identical tandem repeats.
316 The rigidity and size of Rubisco holoenzymes previously enabled the determination of their
317 positions and orientations within the pyrenoid matrix of native cells by cryo-electron
318 tomography⁵. The identification of EPYC1 binding sites on Rubisco in the present work and the
319 modeling of linker regions between EPYC1's Rubisco binding regions now make the
320 *Chlamydomonas* pyrenoid matrix one of the most structurally well-defined phase-separated
321 organelles. Thus, beyond advancing our structural understanding of pyrenoids, organelles that
322 play a central role in the global carbon cycle, we hope that the findings presented here will also
323 more broadly enable advances in the biophysical understanding of phase-separated organelles.

324 **Methods**

325

326 **Strains and culture conditions**

327 Chlamydomonas wild-type (WT) strain cMJ030 was maintained in the dark or low light (~10
328 $\mu\text{mol photons m}^{-2} \text{ s}^{-1}$) on 1.5% agar plates containing Tris-Acetate-Phosphate medium with
329 revised trace elements³³. For Rubisco extraction, 500 mL Tris-Acetate-Phosphate medium in a 1
330 L flask was inoculated with a loopful of cells and the culture was grown to 4×10^6 cells/mL at
331 22°C, shaking at 200 rpm under ~100 $\mu\text{mol photons m}^{-2} \text{ s}^{-1}$ white light in 3% CO₂.
332 Chlamydomonas mutant T60-3³⁴ ($\Delta rbcS$; containing a deletion of both *RBCS* genes) was used for
333 generating Rubisco small subunit point mutants and a wild-type control in the same background.
334 This strain was maintained on agar in the dark or low light (~10 $\mu\text{mol photons m}^{-2}\text{s}^{-1}$).

335

336 **Protein extraction**

337 Rubisco was purified from Chlamydomonas strain cMJ030³⁵. Cells were disrupted by
338 ultrasonication in lysis buffer (10 mM MgCl₂, 50 mM Bicine, 10 mM NaHCO₃, 1 mM
339 dithiothreitol, pH 8.0) supplemented with Halt Protease Inhibitor Cocktail, EDTA-Free (Thermo
340 Fisher Scientific). The soluble lysate was fractionated by ultracentrifugation on a 10-30%
341 sucrose gradient in a SW 41 Ti rotor at a speed of 35,000 rpm for 20 hours at 4°C. Rubisco-
342 containing fractions were applied to an anion exchange column (MONO Q 5/50 GL, GE
343 Healthcare) and eluted with a linear salt gradient from 30 to 500 mM NaCl in lysis buffer.

344

345 **Peptide arrays**

346 Peptide arrays were purchased from the MIT Biopolymers Laboratory (Cambridge, MA). The
347 tiling array was composed of 18-amino-acid peptides that tiled across the full-length EPYC1
348 sequence with a step size of one amino acid. Each peptide was represented by at least two spots
349 on the array, and these replicates were averaged during data analysis. The locations of peptides
350 on the array were randomized. In the substitution arrays, peptides were designed to represent
351 every possible one-amino-acid mutation of the indicated region on EPYC1 by substitution with
352 one of the other 19 amino acids. The arrays were activated by methanol, then washed 3x10 min
353 in binding buffer (50 mM HEPES, 50 mM KOAc, 2 mM Mg(OAc)₂·4H₂O, 1 mM CaCl₂ and 200
354 mM sorbitol, pH 6.8). The arrays were then incubated at 4°C with 1 mg purified Rubisco

355 overnight. The arrays were washed in binding buffer to remove any unbound Rubisco. Using a
356 semi-dry transfer apparatus (BIO-RAD), bound Rubisco was transferred onto an Immobilon-P
357 PVDF membrane (Millipore Sigma). The Rubisco was detected by one of two methods: western
358 blotting, or fluorescent labeling. While replicates using the two methods gave similar results,
359 toward the end of the project we found that fluorescent labeling had a lower background, so we
360 show fluorescent labeling data in Figure 1; all other data were obtained by western blotting and
361 chemiluminescence. For fluorescent labeling, Rubisco was labeled with Alexa Fluor™ 680 dye
362 (Thermo Fisher Scientific) and detected by Typhoon Scanner (GE Healthcare). For western
363 blotting, Rubisco was immuno-detected with a polyclonal primary antibody raised against
364 Rubisco¹⁵ (1:10,000) followed by a HRP conjugated goat anti-rabbit (1:20,000; Invitrogen), and
365 the chemiluminescence was detected by ImageQuant LAS 4000 (GE Healthcare). Images were
366 analyzed with ImageQuant TL (GE Healthcare). Arrays were stripped with Restore™ Western
367 Blot Stripping Buffer before re-use (Thermo Fisher Scientific).

368 For both types of arrays, values for identical sequences present multiple times were
369 averaged. For tiling arrays, the average value for each sequence was plotted at its position in
370 EPYC1 (or at multiple positions for sequences present multiple times). For amino acid
371 substitution arrays, the ratio of each substitution sequence to the corresponding wildtype
372 sequence was calculated and arrayed by amino acid and position.

373

374 **Surface plasmon resonance (SPR) experiments**

375 All the surface preparation experiments were performed at 25°C using a Biacore 3000 instrument
376 (GE Healthcare). Purified Rubisco was immobilized on CM5 sensor chips using a Biacore
377 Amine Coupling Kit according to the manufacturer's instructions. Briefly, the chip surface was
378 activated by an injection of 1:1 N-hydroxysuccinimide (NHS)/1-ethyl-3-(3-
379 dimethylaminopropyl)carbodiimide hydrochloride (EDC). Rubisco was diluted to ~100 µg/mL in
380 10 mM acetate (pH 4.5; this pH had been previously optimized using the immobilization pH
381 scouting wizard) and was injected over the chip surface. Excess free amine groups were then
382 capped with an injection of 1 M ethanolamine. Typical immobilization levels were 8,000 to
383 10,000 resonance units (RU), as recommended for binding experiments of small molecules. For
384 kinetic experiments (for determining the binding affinities), the typical immobilization levels
385 were ~5,000 RU. The control surfaces were prepared in exactly the same manner as the

386 experimental surfaces except that no Rubisco was injected. For immobilizations, the running
387 buffer was the Biacore HBS-EP Buffer (0.01 M HEPES pH 7.4, 0.15 M NaCl, 3 mM EDTA,
388 0.005% v/v Surfactant P20).

389 All the binding assays were performed using the Biacore PBS-P+ Buffer (20 mM
390 phosphate buffer, 2.7 mM KCl, 137 mM NaCl and 0.05% Surfactant P20, pH 6.8) as a running
391 buffer, as recommended for small molecule analysis in Biacore systems. The analytes, consisting
392 of EPYC1 peptides synthesized by Genscript (Piscataway, New Jersey), were dissolved in the
393 same running buffer and diluted to 1 mM. The analytes were injected over the control surface
394 and experimental surfaces at a flow rate of 26 $\mu\text{L}/\text{min}$ for 2.5 minutes, followed by 2.5 minutes
395 of the running buffer alone to allow for dissociation. The surfaces were then regenerated using
396 running buffer at a flow rate of 30 $\mu\text{L}/\text{min}$ for 10 minutes. In all cases, binding to the control
397 surface was negligible.

398 For determining the K_D of EPYC1 peptide, the kinetic assays were performed with a
399 running buffer consisting of 200 mM sorbitol, 50 mM HEPES, 50 mM KOAc, 2 mM
400 $\text{Mg}(\text{OAc})_2 \cdot 4\text{H}_2\text{O}$ and 1 mM CaCl_2 at pH 6.8 (the same buffer as the peptide array assay). The
401 EPYC1 peptide was dissolved in the same running buffer as the assay and the serial dilutions
402 were also made in the same buffer. The analytes were injected over the control surface and
403 experimental surfaces at a flow rate of 15 $\mu\text{L}/\text{min}$ for 2 minutes, followed by 10 minutes with the
404 running buffer alone to allow for dissociation. The surfaces were then regenerated by the running
405 buffer at a flow rate of 30 $\mu\text{L}/\text{min}$ for 10 minutes. In all cases, binding to the blank chip was
406 negligible. The fitting and modeling were performed with the BIAevaluation software.

407

408 **Single-particle cryo-electron microscopy data collection and image processing**

409 Rubisco and EPYC1₄₉₋₇₂ peptides with the final concentrations of 1.69 mg/ml ($=3.02 \mu\text{M}$) and
410 7.5 mM, respectively, were incubated together on ice for 20 minutes in buffer consisting of 200
411 mM sorbitol, 50 mM HEPES, 50 mM KOAc, 2 mM $\text{Mg}(\text{OAc})_2 \cdot 4\text{H}_2\text{O}$ and 1 mM CaCl_2 at pH 6.8
412 (the same buffer as the peptide array assay and the SPR binding assay). Rubisco and EPYC1₁₀₆₋
413 ₁₃₅ peptides with the final concentrations of 1.75 mg/ml ($=3.13 \mu\text{M}$) and 10 mM, respectively,
414 were incubated together on ice for 20 minutes in the same buffer described above. For apo
415 Rubisco and Rubisco incubated with peptides, similar cryo grid-making procedures were used.
416 400-mesh Quantifoil 1.2/1.3 Cu grids (Quantifoil, Großlobichau, Germany) were made

417 hydrophilic by glow discharging for 60 seconds with a current of 15 mA in a PELCO easiGlow
418 system. Cryo grids were produced using a FEI Mark IV Vitrobot (FEI company, part of Thermo
419 Fisher Scientific, Hillsboro, OR). The chamber of the Vitrobot was kept at 4°C and 100%
420 relative humidity. 3 μ l of sample was applied to the glow-discharged grid and blotted with filter
421 paper for 3 seconds with the equipment-specific blotting force set at 3. After blotting, the grid
422 was rapidly plunge-frozen into a liquid ethane bath.

423 For apo Rubisco and Rubisco incubated with EPYC1₄₉₋₇₂ peptide, cryo grids were loaded
424 into a 300 kV FEI Titan Krios cryo electron microscope (FEI Company) at HHMI Janelia
425 Research Campus, Janelia Krios2, equipped with a Gatan K2 Summit camera. After initial
426 screening and evaluation, fully automated data collection was carried out using SerialEM. The
427 final exposure from each collection target was collected as a movie utilizing dose fractionation
428 on the K2 Summit camera operated in super-resolution mode. The movies were collected at a
429 calibrated magnification of 38,168x, corresponding to 1.31 Å per physical pixel in the image
430 (0.655 Å per super-resolution pixel). The dose rate on the specimen was set to be 5.82 electrons
431 per Å² per second and total exposure time was 10 s, resulting in a total dose of 58.2 electrons per
432 Å². With dose fractionation set at 0.2 s per frame, each movie series contained 50 frames and
433 each frame received a dose of 1.16 electrons per Å². The spherical aberration constant of the
434 objective lens is 2.7 mm and an objective aperture of 100 μ m was used. The nominal defocus
435 range for the automated data collection was set to be between -1.5 μ m and -3.0 μ m. For Rubisco
436 incubated with EPYC1₁₀₆₋₁₃₅ peptide, the final exposure was collected on Janelia Krios1
437 equipped with a C_s-corrector, a Gatan Bioquantum energy filter and a post-filter K3 camera. The
438 movies were collected at a nominal magnification of 81,000x, corresponding to 0.844 Å per
439 physical pixel in the image (0.422 Å per super-resolution pixel). The dose rate on the specimen
440 was set to be 12 electrons per pixel per second and total exposure time was 3.56 s, resulting in a
441 total dose of 60 electrons per Å². Each movie series contained 60 frames and each frame
442 received a dose of 1 electron per Å². The nominal defocus range for the automated data
443 collection was set to be between -1 μ m and -1.6 μ m.

444 The movies were 2x binned and motion corrected using MotionCor2³⁶ and CTF was
445 estimated using CTFFIND³⁷ in Relion³⁸. 1,809,869 EPYC1₄₉₋₇₂ peptide-bound Rubisco particles,
446 2,257,131 EPYC1₁₀₆₋₁₃₅ peptide-bound Rubisco particles, and 677,071 Rubisco particles in the
447 apo state were selected using cisTEM³⁹. 2D classification was performed using cisTEM. The

448 classes presenting detailed features in class averages were chosen for 3D classification on
449 cryoSPARC^{40,41} and on Relion. The 3D class showing clear secondary structures was chosen for
450 3D auto-refine first without symmetry and then with D4 symmetry imposed. After CTF
451 refinement and Bayesian polishing in Relion, the reconstructed map resolution is 2.68 Å for the
452 apo state, 2.62 Å for the EPYC1₄₉₋₇₂ peptide-bound state, and 2.06 Å for the EPYC1₁₀₆₋₁₃₅
453 peptide-bound state. The EPYC1₄₉₋₇₂ peptide-bound particles at super-resolution pixel size were
454 further subjected to CTF refinement and polishing, resulting in map at 2.13 Å resolution. Details
455 for single-particle cryo-EM data collection and image processing are included in the
456 Supplementary Table 1.

457

458 **Single-particle cryo-electron microscopy model building, fitting, and refinement**

459 A full model for Rubisco from *Chlamydomonas* was produced from an X-ray structure¹³ (PDB
460 entry 1GK8) and used for rigid body fitting into a local resolution filtered apo or EPYC1₄₉₋₇₂
461 peptide-bound Rubisco cryo-EM map using UCSF Chimera⁴². After rigid body fitting of the full
462 complex, initial flexible fitting was performed in COOT⁴³ by manually going through the entire
463 peptide chain of a single large and small Rubisco subunit before applying the changes to the
464 other seven large and small subunits. The C-terminal part of the small subunit was built manually
465 and the sequences updated to the RBCS2 sequences. The sequence of the EPYC1₄₉₋₇₂ peptide
466 was used to predict secondary structure elements using JPred4⁴⁴, which gave the prediction that
467 the C-terminal region (NWRQELES) is α -helical. Guided by this prediction, the peptide was
468 built manually into the density using COOT. Additional maps like the initial 2.62 Å from the
469 binned data and maps filtered to different resolutions with various applied B-factors were also
470 used to help with model building in unclear regions. Additional real space refinement of the
471 entire complex was performed using Phenix⁴⁵. The EPYC1₁₀₆₋₁₃₅ peptide bound map was used to
472 build a model of the EPYC1₁₀₆₋₁₃₅ peptide. First rigid body fitting of the EPYC1₄₉₋₇₂ peptide-
473 bound Rubisco model into a local resolution filtered EPYC1₁₀₆₋₁₃₅ peptide-bound Rubisco cryo-
474 EM map was performed using UCSF Chimera. Then the sequence of the peptide was mutated to
475 the EPYC1₁₀₆₋₁₃₅ peptide sequence, followed by flexible fitting to slightly adjust the PDB to the
476 density. Models were subjected to an all-atom structure validation using MolProbity⁴⁶. Figures
477 were produced using UCSF Chimera.

478

479 **Liquid–liquid phase separation assay**

480 Proteins used in the liquid–liquid phase separation assay were obtained and stored essentially as
481 described previously¹¹. Briefly, Rubisco was purified from *Chlamydomonas reinhardtii* cells
482 (CC-2677 cw15 nit1-305 mt-5D, Chlamydomonas Resource Center), grown in Sueoka’s high-
483 salt medium⁴⁷, using a combination of anion exchange chromatography and gel filtration.

484 The EPYC1 full-length gene (encoding amino acids 1-317) and corresponding R/K
485 mutant (EPYC1^{R64A/K127A/K187A/K248A/R314A}) were synthesized by GenScript and cloned between
486 the SacII and HindIII site of the pHue vector⁴⁸. Proteins were produced in the *E. coli* strain BL21
487 (DE3) harbouring pBADESL⁴⁹ for co-expression of the *E. coli* chaperonin GroEL/S. The
488 purification was conducted with minor changes (dialysis for removal of high imidazol
489 concentrations was skipped by running the gel-filtration column before the second IMAC). After
490 the first IMAC step and cleavage⁵⁰ of the N-terminal His₆-ubiquitin tag, proteins were separated
491 by gel filtration. Finally, the peak fraction was passed a second time through an IMAC column,
492 collecting EPYC1 from the flow through.

493 EPYC1-Rubisco condensates were reconstituted *in vitro* in a buffer containing 20 mM
494 Tris-HCl (pH 8.0) and NaCl concentrations as indicated. 5 µl reactions were incubated for 3
495 minutes at room temperature before monitoring the droplet formation by differential interference
496 contrast (DIC) microscopy. DIC images were acquired with a Nikon Eclipse Ti Inverted
497 Microscope using a 60× oil-immersion objective after allowing the droplets to settle on the
498 coverslip (Superior Marienfeld, Germany) surface for about 3 minutes. For droplet sedimentation
499 assays 10 µl reactions were incubated for 3 minutes at 20°C before separating the droplets from
500 the bulk phase by spinning for 3 minutes at 21,000xg and 4°C. Pelleted droplets and supernatant
501 fractions were analyzed using Coomassie-stained SDS-PAGE.

502

503 **Yeast two-hybrid assay**

504 Yeast two-hybrid to detect interactions between EPYC1 and RbcS1 was carried out as described
505 previously¹². EPYC1 was cloned into the two-hybrid vector pGBKT7 to create a fusion with the
506 GAL4 DNA binding domain. Point mutations were introduced by PCR into RbcS1, which was
507 then cloned in the pGADT7 to create a fusion with the GAL4 activation domain. Yeast cells
508 were then co-transformed with binding and activation domain vectors. Successful transformants
509 were cultured, diluted to an optical density at 600 nm (OD600) of 0.5 or 0.1, and plated onto SD-

510 L-W and SD-L-W-H containing increasing concentrations of the HIS3 inhibitor triaminotriazole
511 (3-AT). Plates were imaged after 3 days. Spots shown in Fig. 5a were grown at 5 mM 3-AT from
512 a starting OD600 of 0.5; they are a subset of the full dataset shown in Extended Data Fig. 6.

513

514 **Cloning of Rubisco small subunit point mutants**

515 The plasmid pSS1-ITP⁵¹ which contains *Chlamydomonas RBCS1* including UTRs and introns 1
516 and 2 was used as a starting point for generating plasmids pSH001 and pSH002, which encode
517 *RBCS1*^{D23A/E24A}, and *RBCS1*^{M87D/V94D}, respectively. The point mutations were generated by
518 Gibson assembly⁵² of gBlocks (synthesized by Integrated DNA Technologies) containing the
519 desired mutations into pSS-ITP that had been enzyme digested by restriction endonucleases
520 (XcmI and BbvCI for the D23A/E24A mutations and BbvCI and BlnI for the M87D/V94D
521 mutations). All constructs were verified by Sanger sequencing.

522 The fragment for making pSH001 (containing the D23A/E24A Rubisco small subunit
523 mutant) had the following sequence:

```
524 GCAGGGCTGCCCCGGCTCAGGCCAACCAGATGATGGTCTGGACCCCGGTCAACAAC  
525 AAGATGTTTCGAGACCTTCTCCTACCTGCCTCCTCTGACCGCCGCGCAGATCGCCGCC  
526 CAGGTCGACTACATCGTCGCCAACGGCTGGATCCCCTGCCTGGAGTTCGCTGAGGCC  
527 GACAAGGCCTACGTGTCCAAC
```

528 The fragment for making pSH002 (containing the M87D/V94D Rubisco small subunit
529 mutant) had the following sequence:

```
530 CTGCCTGGAGTTCGCTGAGGCCGACAAGGCCTACGTGTCCAACGAGTCGGCCATCC  
531 GCTTCGGCAGCGTGTCTTGCCTGTACTACGACAACCGCTACTGGACCATGTGGAAGC  
532 TGCCCATGTTTCGGCTGCCGCGACCCCGACCAGGTGCTGCGCGAGATCGACGCCTGCA  
533 CCAAGGCCTTCCCCGATGCCTACGTGCGCCTGGTGGCCTTCGACAACCAGAAGCAG  
534 GTGCAGATCATGGGCTTCTGGTCCAGCGCCCCAAGACTGCCCGCGACTTCCAGCCC  
535 GCCAACAAGCGCTCCGTGTAAATGGAGGCGCTCGTCGATCTGAGCCGTGTGTGATGT  
536 TTGTTGGTGTGTTGAGCGAGTGCAATGAGAGTGTGTGTGTGTGTTGTTGGTGTGTG  
537 GCTAAGCCAAGCGTGATCGC
```

538 Both the plasmids pSH001 and pSH002 have been submitted to the *Chlamydomonas*
539 Resource Center (www.chlamycollection.org).

540

541 **Transformation of Chlamydomonas to make the Rubisco small subunit point mutants**

542 Chlamydomonas strains $\Delta rbcS;RBCS^{WT}$, $\Delta rbcS;RBCS^{D23A/E24A}$, and $\Delta rbcS;RBCS^{M87D/V94D}$ (The
543 accession numbers of these strains in Chlamydomonas Resource Center are CC-5616, CC-5617
544 and CC-5618, respectively.) were generated by transforming pSS1-ITP, pSH001, and pSH002
545 (encoding Rubisco small subunit constructs) into the Rubisco small subunit deletion mutant T60
546 ($\Delta rbcS$) by electroporation as described previously⁵³. For each transformation, 29 ng kbp⁻¹ of
547 KpnI linearized plasmid was mixed with 250 μ L of 2×10^8 cells mL⁻¹ at 16°C and electroporated
548 immediately. Transformant colonies were selected on Tris-Phosphate plates without antibiotics
549 at 3% v/v CO₂ under ~ 50 μ mol photons m⁻² s⁻¹ light. The sequence of RbcS in the transformants
550 was verified by PCR amplification and Sanger sequencing.

551

552 **Spot tests**

553 $\Delta rbcS;RBCS^{WT}$, $\Delta rbcS;RBCS^{D23A/E24A}$, and $\Delta rbcS;RBCS^{M87D/V94D}$ (The accession numbers of these
554 strains in Chlamydomonas Resource Center are CC-5616, CC-5617 and CC-5618, respectively.)
555 were grown in Tris-Phosphate medium at 3% CO₂ until $\sim 2 \times 10^6$ cells mL⁻¹. Cells were diluted in
556 Tris-Phosphate medium to a concentration of 8.7×10^7 cells mL⁻¹, then serially diluted 1:10 three
557 times. 7.5 μ L of each dilution was spotted onto four TP plates and incubated in air or 3% CO₂
558 under 20 or 100 μ mol photons m⁻² s⁻¹ white light for 9 days before imaging.

559

560 **Transmission electron microscopy**

561 Samples for electron microscopy were fixed for 1 hour at room temperature in 2.5%
562 glutaraldehyde in Tris-Phosphate medium (pH 7.4), followed by 1 hour at room temperature in
563 1% OsO₄, 1.5% K₃Fe(CN)₃, and 2 mM CaCl₂. Fixed cells were then bulk stained for 1 hour in
564 2% uranyl acetate, 0.05 M maleate buffer at pH 5.5. After serial dehydration (50%, 75%, 95%,
565 and 100% ethanol, followed by 100% acetonitrile), samples were embedded in epoxy resin
566 containing 34% Quetol 651, 44% nonenyl succinic anhydride, 20% methyl-5- norbornene-2,3-
567 dicarboxylic anhydride, and 2% catalyst dimethylbenzylamine. Ultramicrotomy was done by the
568 Core Imaging Lab, Medical School, Rutgers University. Imaging was performed at the Imaging
569 and Analysis Center, Princeton University, on a CM100 transmission electron microscope
570 (Philips, Netherlands) at 80 kV.

571

572 **Measurement of nearest-neighbor distances between EPYC1 binding sites on Rubisco**
573 **holoenzymes within pyrenoids**

574 For detailed descriptions of the *Chlamydomonas* cell culture, vitrification of cells onto EM grids,
575 thinning of cells by cryo-focused ion beam milling, 3D imaging of native pyrenoids by cryo-
576 electron tomography, tomographic reconstruction, template matching, and subtomogram
577 averaging, see our previous study⁵. In that study, we measured the distances between the center
578 positions of Rubisco complexes within tomograms of five pyrenoids. The spatial parameters
579 determined in that study were combined with the EPYC1-binding sites resolved here by cryo-
580 EM single-particle analysis to measure the nearest-neighbor distances between EPYC1 binding
581 sites on adjacent Rubisco complexes within the native pyrenoid matrix.

582 The *in situ* subtomogram average EMD-3694⁵ was used as the reference for the Rubisco
583 model. We extracted the isosurface from this density using the 0.5 contour level recommended in
584 the Electron Microscopy Data Bank entry. We then fit the atomic model of EPYC1-bound
585 Rubisco (Fig. 2) within the EMD-3694 density, and for each EPYC1 binding site, we marked the
586 closest point on the isosurface to define the EPYC1 binding sites on this model. The positions
587 and orientations previously determined by subtomogram averaging were used to place each
588 Rubisco model and its corresponding binding sites into the pyrenoid tomograms using the PySeg
589 program⁵⁴.

590 To compute the nearest-neighbor distances between EPYC1 binding sites on two
591 different Rubisco complexes, first, linkers were drawn between each EPYC1 binding site and all
592 other binding sites within 25 nm. Binding sites on the same Rubisco complex were ignored.
593 Next, the linkers were filtered by length (defined as the Euclidean distance between the two
594 binding sites), and only the shortest linker was retained for each binding site. To prevent edge
595 effects, linkers were discarded if they had a binding site <12 nm from the masked excluded
596 volume (grey in Fig. 6b), which marks the border of the analyzed pyrenoid matrix. Finally, linker
597 distances were plotted in a histogram to show the distribution of lengths (normalized to 100%).

598 Regarding the accuracy of the Rubisco localization in the previous study⁵, we used
599 template matching, subtomogram alignment, and hierarchical classification to identify 97.5% of
600 the Rubisco complexes in each of the five pyrenoid volumes. The Rubisco average was
601 determined at a resolution of 16.5 Å. This could be interpreted to mean that the Rubisco
602 complexes were localized with 1.65 nm precision. However, this resolution is not a simple

603 reflection of translational and rotational accuracy, but is also greatly limited by the contrast
604 transfer function and pixel size of the tomographic data. Furthermore, with this localization
605 uncertainty being random for each particle, it would not change the ~4 nm peak distance between
606 neighboring EPYC1 binding sites measured in our current study.

607

608 **Modeling of the energy required to stretch EPYC1-linker regions**

609 The energy required to stretch the linker regions between EPYC1's Rubisco-binding regions was
610 determined as follows. The force F required to stretch a 40 amino acid linker region to any given
611 length z was approximated using a wormlike chain model⁵⁵:

$$F(z) = \frac{k_B T}{4L_p} \left[\frac{1}{(1 - z/L_0)^2} - 1 + \frac{4z}{L_0} \right]$$

612 In the above equation, k_B is the Boltzmann constant, T is the temperature, L_p is the persistence
613 length (assumed to be 1 nm, a representative value for disordered proteins), and L_0 is the contour
614 length (estimated as 40 amino acids * 0.36 nm/amino acid). The energy required to stretch the
615 linker to a length x is given by:

$$E(x) = \int_0^x F(z) dz$$

616 This energy was calculated and plotted in Fig. 6d.

617

618 **Data availability**

619 All data generated or analyzed during this study are included in this Article, the Extended Data
620 and the Supplementary tables. The single-particle cryo-EM maps have been deposited in the
621 Electron Microscopy Data Bank with accession codes EMDB-22401, EMDB-22308 and EMDB-
622 22462. The atomic models have been deposited in the Protein Data Bank under accession codes
623 PDB 7JN4, PDB 7JFO and PDB 7JSX. The raw datasets have been deposited in the Electron
624 Microscopy Public Image Archive with accession codes EMPIAR-10503, EMPIAR-10502 and
625 EMPIAR-10501. The subtomogram average of Rubisco has been deposited in the Electron
626 Microscopy Data Bank with accession code EMD-3694.

627

628 **References**

- 629 1 Field, C. B., Behrenfeld, M. J., Randerson, J. T. & Falkowski, P. Primary production of
630 the biosphere: integrating terrestrial and oceanic components. *Science* **281**, 237-240
631 (1998).
- 632 2 Hessler, A. M., Lowe, D. R., Jones, R. L. & Bird, D. K. A lower limit for atmospheric
633 carbon dioxide levels 3.2 billion years ago. *Nature* **428**, 736-738 (2004).
- 634 3 Ainsworth, E. A. & Long, S. P. What have we learned from 15 years of free-air CO₂
635 enrichment (FACE)? A meta-analytic review of the responses of photosynthesis, canopy
636 properties and plant production to rising CO₂. *New Phytol* **165**, 351-371,
637 doi:10.1111/j.1469-8137.2004.01224.x (2005).
- 638 4 Raven, J. A., Cockell, C. S. & De La Rocha, C. L. The evolution of inorganic carbon
639 concentrating mechanisms in photosynthesis. *Philosophical transactions of the Royal
640 Society of London. Series B, Biological sciences* **363**, 2641-2650,
641 doi:10.1098/rstb.2008.0020 (2008).
- 642 5 Freeman Rosenzweig, E. S. *et al.* The Eukaryotic CO₂-Concentrating Organelle Is
643 Liquid-like and Exhibits Dynamic Reorganization. *Cell* **171**, 148-162 e119,
644 doi:10.1016/j.cell.2017.08.008 (2017).
- 645 6 Badger, M. R. *et al.* The diversity and coevolution of Rubisco, plastids, pyrenoids, and
646 chloroplast-based CO₂-concentrating mechanisms in algae. *Can J Bot* **76**, 1052–1071,
647 doi:10.1139/b98-074 (1998).
- 648 7 Villarreal, J. C. & Renner, S. S. Hornwort pyrenoids, carbon-concentrating structures,
649 evolved and were lost at least five times during the last 100 million years. *Proc Natl Acad
650 Sci U S A* **109**, 18873-18878, doi:10.1073/pnas.1213498109 (2012).
- 651 8 Wang, Y., Stessman, D. J. & Spalding, M. H. The CO₂ concentrating mechanism and
652 photosynthetic carbon assimilation in limiting CO₂ : how *Chlamydomonas* works against
653 the gradient. *The Plant journal : for cell and molecular biology* **82**, 429-448,
654 doi:10.1111/tpj.12829 (2015).
- 655 9 Raven, J. A. CO₂-concentrating mechanisms: A direct role for thylakoid lumen
656 acidification? *Plant Cell Environ* **20**, 147-154, doi:Doi 10.1046/J.1365-3040.1997.D01-
657 67.X (1997).
- 658 10 Mackinder, L. C. *et al.* A repeat protein links Rubisco to form the eukaryotic carbon-
659 concentrating organelle. *Proc Natl Acad Sci U S A* **113**, 5958-5963,
660 doi:10.1073/pnas.1522866113 (2016).

- 661 11 Wunder, T., Cheng, S. L. H., Lai, S. K., Li, H. Y. & Mueller-Cajar, O. The phase
662 separation underlying the pyrenoid-based microalgal Rubisco supercharger. *Nature*
663 *communications* **9**, 5076, doi:10.1038/s41467-018-07624-w (2018).
- 664 12 Atkinson, N. *et al.* The pyrenoidal linker protein EPYC1 phase separates with hybrid
665 Arabidopsis-Chlamydomonas Rubisco through interactions with the algal Rubisco small
666 subunit. *Journal of experimental botany* **70**, 5271-5285, doi:10.1093/jxb/erz275 (2019).
- 667 13 Taylor, T. C., Backlund, A., Bjorhall, K., Spreitzer, R. J. & Andersson, I. First crystal
668 structure of Rubisco from a green alga, *Chlamydomonas reinhardtii*. *J Biol Chem* **276**,
669 48159-48164, doi:10.1074/jbc.M107765200 (2001).
- 670 14 Duff, A. P., Andrews, T. J. & Curmi, P. M. The transition between the open and closed
671 states of rubisco is triggered by the inter-phosphate distance of the bound bisphosphate. *J*
672 *Mol Biol* **298**, 903-916, doi:10.1006/jmbi.2000.3724 (2000).
- 673 15 Meyer, M. T. *et al.* Rubisco small-subunit α -helices control pyrenoid formation in
674 *Chlamydomonas*. *Proc Natl Acad Sci U S A* **109**, 19474-19479,
675 doi:10.1073/pnas.1210993109. (2012).
- 676 16 Engel, B. D. *et al.* Native architecture of the *Chlamydomonas* chloroplast revealed by in
677 situ cryo-electron tomography. *eLife* **4**, DOI: 10.7554/eLife.04889,
678 doi:10.7554/eLife.04889 (2015).
- 679 17 Goodenough, U. W. & Levine, R. P. Chloroplast structure and function in ac-20, a
680 mutant strain of *Chlamydomonas reinhardtii*. 3. Chloroplast ribosomes and membrane
681 organization. *J Cell Biol.* **44**, 547-562, doi:10.1083/jcb.44.3.547 (1970).
- 682 18 Ma, Y., Pollock, S. V., Xiao, Y., Cunnusamy, K. & Moroney, J. V. Identification of a
683 novel gene, CIA6, required for normal pyrenoid formation in *Chlamydomonas*
684 *reinhardtii*. *Plant Physiol* **156**, 884-896, doi:10.1104/pp.111.173922 (2011).
- 685 19 Caspari, O. D. *et al.* Pyrenoid loss in *Chlamydomonas reinhardtii* causes limitations in
686 CO₂ supply, but not thylakoid operating efficiency. *Journal of experimental botany* **68**,
687 3903-3913, doi:10.1093/jxb/erx197 (2017).
- 688 20 Li, P. *et al.* Phase transitions in the assembly of multivalent signalling proteins. *Nature*
689 **483**, 336-340, doi:10.1038/nature10879 (2012).
- 690 21 Borkhsenius, O. N., Mason, C. B. & Moroney, J. V. The Intracellular Localization of
691 Ribulose-1,5-Bisphosphate Carboxylase/Oxygenase in *Chlamydomonas reinhardtii*. *Plant*
692 *Physiol* **116**, 1585–1591, doi:10.1104/pp.116.4.1585 (1998).
- 693 22 Turkina, M. V., Blanco-Rivero, A., Vainonen, J. P., Vener, A. V. & Villarejo, A. CO₂
694 limitation induces specific redox-dependent protein phosphorylation in *Chlamydomonas*
695 *reinhardtii*. *Proteomics* **6**, 2693-2704, doi:10.1002/pmic.200500461 (2006).

- 696 23 Cai, F. *et al.* Advances in Understanding Carboxysome Assembly in Prochlorococcus and
697 Synechococcus Implicate CsoS2 as a Critical Component. *Life (Basel)* **5**, 1141-1171,
698 doi:10.3390/life5021141 (2015).
- 699 24 Oltrogge, L. M. *et al.* Multivalent interactions between CsoS2 and Rubisco mediate
700 alpha-carboxysome formation. *Nat Struct Mol Biol* **27**, 281-287, doi:10.1038/s41594-
701 020-0387-7 (2020).
- 702 25 Long, B. M., Badger, M. R., Whitney, S. M. & Price, G. D. Analysis of carboxysomes
703 from Synechococcus PCC7942 reveals multiple Rubisco complexes with carboxysomal
704 proteins CcmM and CcaA. *J Biol Chem* **282**, 29323-29335, doi:10.1074/jbc.M703896200
705 (2007).
- 706 26 Wang, H. *et al.* Rubisco condensate formation by CcmM in beta-carboxysome
707 biogenesis. *Nature* **566**, 131-135, doi:10.1038/s41586-019-0880-5 (2019).
- 708 27 Hennacy, J. H. & Jonikas, M. C. Prospects for Engineering Biophysical CO₂
709 Concentrating Mechanisms into Land Plants to Enhance Yields. *Annual review of plant*
710 *biology*, doi:10.1146/annurev-arplant-081519-040100 (2020).
- 711 28 Long, B. M. *et al.* Carboxysome encapsulation of the CO₂-fixing enzyme Rubisco in
712 tobacco chloroplasts. *Nature communications* **9**, 3570, doi:10.1038/s41467-018-06044-0
713 (2018).
- 714 29 Lin, M. T., Occhialini, A., Andralojc, P. J., Parry, M. A. & Hanson, M. R. A faster
715 Rubisco with potential to increase photosynthesis in crops. *Nature* **513**, 547-550,
716 doi:10.1038/nature13776 (2014).
- 717 30 Atkinson, N. *et al.* Introducing an algal carbon-concentrating mechanism into higher
718 plants: location and incorporation of key components. *Plant Biotechnol J* **14**, 1302-1315,
719 doi:10.1111/pbi.12497 (2016).
- 720 31 Hanson, M. R., Gray, B. N. & Ahner, B. A. Chloroplast transformation for engineering of
721 photosynthesis. *Journal of experimental botany* **64**, 731-742, doi:10.1093/jxb/ers325
722 (2013).
- 723 32 Raven, J. A., Beardall, J. & Sanchez-Baracaldo, P. The possible evolution and future of
724 CO₂-concentrating mechanisms. *J Exp Bot* **68**, 3701-3716, doi:10.1093/jxb/erx110
725 (2017).
- 726 33 Kropat, J. *et al.* A revised mineral nutrient supplement increases biomass and growth rate
727 in *Chlamydomonas reinhardtii*. *The Plant journal : for cell and molecular biology* **66**,
728 770-780, doi:10.1111/j.1365-313X.2011.04537.x (2011).
- 729 34 Khrebtukova, I. & Spreitzer, R. J. Elimination of the Chlamydomonas gene family that
730 encodes the small subunit of ribulose-1,5-bisphosphate carboxylase/oxygenase. *Proc Natl*
731 *Acad Sci U S A* **93**, 13689-13693, doi:10.1073/pnas.93.24.13689 (1996).

- 732 35 Zhang, R. *et al.* High-Throughput Genotyping of Green Algal Mutants Reveals Random
733 Distribution of Mutagenic Insertion Sites and Endonucleolytic Cleavage of Transforming
734 DNA. *Plant Cell* **26**, 1398-1409, doi:10.1105/tpc.114.124099 (2014).
- 735 36 Zheng, S. Q. *et al.* MotionCor2: anisotropic correction of beam-induced motion for
736 improved cryo-electron microscopy. *Nat Methods* **14**, 331-332, doi:10.1038/nmeth.4193
737 (2017).
- 738 37 Rohou, A. & Grigorieff, N. CTFFIND4: Fast and accurate defocus estimation from
739 electron micrographs. *J Struct Biol* **192**, 216-221, doi:10.1016/j.jsb.2015.08.008 (2015).
- 740 38 Zivanov, J. *et al.* New tools for automated high-resolution cryo-EM structure
741 determination in RELION-3. *eLife* **7**, doi:10.7554/eLife.42166 (2018).
- 742 39 Grant, T., Rohou, A. & Grigorieff, N. cisTEM, user-friendly software for single-particle
743 image processing. *eLife* **7**, doi:10.7554/eLife.35383 (2018).
- 744 40 Punjani, A., Rubinstein, J. L., Fleet, D. J. & Brubaker, M. A. cryoSPARC: algorithms for
745 rapid unsupervised cryo-EM structure determination. *Nat Methods* **14**, 290-296,
746 doi:10.1038/nmeth.4169 (2017).
- 747 41 Punjani, A., Brubaker, M. A. & Fleet, D. J. Building Proteins in a Day: Efficient 3D
748 Molecular Structure Estimation with Electron Cryomicroscopy. *IEEE Trans Pattern Anal*
749 *Mach Intell* **39**, 706-718, doi:10.1109/TPAMI.2016.2627573 (2017).
- 750 42 Pettersen, E. F. *et al.* UCSF Chimera--a visualization system for exploratory research and
751 analysis. *J Comput Chem* **25**, 1605-1612, doi:10.1002/jcc.20084 (2004).
- 752 43 Emsley, P., Lohkamp, B., Scott, W. G. & Cowtan, K. Features and development of Coot.
753 *Acta Crystallogr D Biol Crystallogr* **66**, 486-501, doi:10.1107/S0907444910007493
754 (2010).
- 755 44 Drozdetskiy, A., Cole, C., Procter, J. & Barton, G. J. JPred4: a protein secondary
756 structure prediction server. *Nucleic Acids Res* **43**, W389-394, doi:10.1093/nar/gkv332
757 (2015).
- 758 45 Adams, P. D. *et al.* PHENIX: a comprehensive Python-based system for macromolecular
759 structure solution. *Acta Crystallogr D Biol Crystallogr* **66**, 213-221,
760 doi:10.1107/S0907444909052925 (2010).
- 761 46 Chen, V. B. *et al.* MolProbity: all-atom structure validation for macromolecular
762 crystallography. *Acta Crystallogr D Biol Crystallogr* **66**, 12-21,
763 doi:10.1107/S0907444909042073 (2010).
- 764 47 Sueoka, N. Mitotic replication of deoxyribonucleic acid in *Chlamydomonas reinhardi*.
765 *Proc Natl Acad Sci U S A*. **46**, 83-91, doi:10.1073/pnas.46.1.83 (1960).

- 766 48 Catanzariti, A. M., Soboleva, T. A., Jans, D. A., Board, P. G. & Baker, R. T. An efficient
767 system for high-level expression and easy purification of authentic recombinant proteins.
768 *Protein Sci* **13**, 1331-1339, doi:10.1110/ps.04618904 (2004).
- 769 49 Ewalt, K. L., Hendrick, J. P., Houry, W. A. & Hartl, F. U. In vivo observation of
770 polypeptide flux through the bacterial chaperonin system. *Cell* **90**, 491-500,
771 doi:10.1016/s0092-8674(00)80509-7 (1997).
- 772 50 Baker, R. T. *et al.* in *Ubiquitin and Protein Degradation, Part A Methods in Enzymology*
773 540-554 (2005).
- 774 51 Genkov, T., Meyer, M., Griffiths, H. & Spreitzer, R. J. Functional hybrid rubisco
775 enzymes with plant small subunits and algal large subunits: engineered rbcS cDNA for
776 expression in chlamydomonas. *J Biol Chem* **285**, 19833-19841,
777 doi:10.1074/jbc.M110.124230 (2010).
- 778 52 Gibson, D. G. *et al.* Enzymatic assembly of DNA molecules up to several hundred
779 kilobases. *Nature methods* **6**, 343-345, doi:10.1038/nmeth.1318 (2009).
- 780 53 Li, X. *et al.* A genome-wide algal mutant library and functional screen identifies genes
781 required for eukaryotic photosynthesis. *Nat Genet* **51**, 627-635, doi:10.1038/s41588-019-
782 0370-6 (2019).
- 783 54 Martinez-Sanchez, A. *et al.* Template-free detection and classification of membrane-
784 bound complexes in cryo-electron tomograms. *Nat Methods*, doi:10.1038/s41592-019-
785 0675-5 (2020).
- 786 55 Cheng, S., Cetinkaya, M. & Grater, F. How sequence determines elasticity of disordered
787 proteins. *Biophys J* **99**, 3863-3869, doi:10.1016/j.bpj.2010.10.011 (2010).
- 788

789

790 **Acknowledgements**

791 We thank Jianping Wu, Nieng Yan, Luke Mackinder, Cliff Brangwynne and members of the
792 Jonikas laboratory for helpful discussions; Ned Wingreen, Silvia Ramundo, Jessi Hennacy, Eric
793 Franklin and Alexandra Wilson for constructive feedback on the manuscript; Wolfgang
794 Baumeister and Jürgen Plitzko for providing support and cryo-ET instrumentation; and
795 Miroslava Schaffer for help with acquiring the cryo-ET data, previously published in Freeman
796 Rosenzweig *et al.*, 2017. This project was funded by National Science Foundation (IOS-1359682
797 and MCB-1935444), National Institutes of Health (DP2-GM-119137), and Simons Foundation
798 and Howard Hughes Medical Institute (55108535) grants to M.C.J., Deutsche
799 Forschungsgemeinschaft grant (EN 1194/1-1 as part of FOR2092) to B.D.E., Ministry of

800 Education (MOE Singapore) Tier 2 grant (MOE2018-T2-2-059) to O.M.-C., UK Biotechnology
801 and Biological Sciences Research Council (BB/S015531/1) and Leverhulme Trust (RPG-2017-
802 402) grants to A.J.M and N.A., NIH grant R01GM071574 to F.M.H., Deutsche
803 Forschungsgemeinschaft fellowship (PO2195/1-1) to S.A.P., and National Institute of General
804 Medical Sciences of the National Institutes of Health (T32GM007276) training grant to V.K.C..
805 The content is solely the responsibility of the authors and does not necessarily represent the
806 official view of the National Institutes of Health.

807

808 **Author contributions**

809 S.H., P.D.J., V.C., F.M.H., T.W., O.M.-C., B.D.E., and M.C.J. designed experiments. S.H.
810 identified EPYC1's Rubisco-binding regions on EPYC1 by peptide tiling array and SPR. S.H.
811 and S.A.P. prepared the Rubisco and EPYC1 peptide sample for single-particle cryo-EM; S.H.,
812 S.A.P. and G.H. prepared the Rubisco samples for peptide tiling array and surface plasmon
813 resonance. H.-T.C., D.M. and Z.Y. performed Cryo-EM grid preparation, sample screening, data
814 acquisition, image processing, reconstruction and map generation. D.M. and P.D.J. carried out
815 single-particle model building and fitting and refinement. S.H., H.-T.C., D.M., P.D.J., F.M.H.
816 and M.C.J. analyzed the structures. S.H. and W.P. analyzed EPYC1 binding to Rubisco by
817 peptide substitution array and SPR. T.W. performed in vitro reconstitution phase separation
818 experiments. N.A. and A.J.M. performed yeast two-hybrid experiments. S.H. and M.T.M. made
819 Rubisco small subunit point mutants. S.H. performed spot test experiments. M.T.M. performed
820 TEM. A.M.-S. performed the cryo-ET data analysis and modeling. S.H. and M.C.J. wrote the
821 manuscript. All authors read and commented on the manuscript.

822

823 **Conflict of interest statement**

824 Princeton University and HHMI have submitted a provisional patent application on aspects of
825 the findings.

826 **Figures**

827

828 **Fig. 1 | EPYC1 consists of five tandem sequence repeats, each of which contains a Rubisco-**
829 **binding region. a**, A representative (N=15) transmission electron microscopy (TEM) image of a
830 Chlamydomonas cell. Scale bar = 1 μ m. **b**, Cartoon depicting the chloroplast and pyrenoid in the
831 image shown in panel a. The blue dots indicate the location of Rubisco enzymes clustered in the
832 pyrenoid matrix. **c**, We hypothesized that pyrenoid matrix formation is mediated by multivalent
833 interactions between Rubisco and the intrinsically disordered protein EPYC1. **d**, We designed an
834 array of 18 amino acid peptides tiling across the full length EPYC1 sequence. **e**, Incubation of
835 the array with purified Rubisco allows identification of peptides that bind to Rubisco. **f**, Image of
836 the Rubisco binding signal from the peptide tiling array. **g**, The Rubisco binding signal was
837 quantified and plotted for each peptide as a function of the position of the middle of the peptide
838 along the EPYC1 sequence. The initial 26 amino acids of EPYC1 correspond to a chloroplast
839 targeting peptide (cTP), which is not present in the mature protein¹². Results are representative of
840 three independent experiments. **h**, The positions of EPYC1's five sequence repeats are shown to
841 scale with panel g. Predicted α -helical regions are shown as wavy lines. **i**, Primary sequence of
842 EPYC1, with the five sequence repeats aligned. In panels h and i, the regions represented by
843 peptides subsequently used for structural studies are underlined with red lines (EPYC1₄₉₋₇₂) and
844 pink lines (EPYC1₁₀₆₋₁₃₅). EPYC1₁₀₆₋₁₃₅ is an exact match to the underlined sequence of Repeats
845 2 and 4, and has a one-amino acid difference from the corresponding region in Repeat 3 (dashed
846 underline).

847 **Fig. 2 | EPYC1 binds to Rubisco small subunits.** **a**, Peptide EPYC1₄₉₋₇₂, corresponding to the
848 first Rubisco-binding region of EPYC1, was incubated at saturating concentrations with Rubisco
849 prior to single-particle cryo-electron microscopy. **b-e**, Density maps (**b**, **d**) and cartoons (**c**, **e**)
850 illustrate the side views (**b**, **c**) and top views (**d**, **e**) of the density map of the EPYC1 peptide-
851 Rubisco complex. Dashed boxes in panel **b** indicate regions shown in Fig. 3a-f.
852

853 **Fig. 3 | EPYC1 binds to Rubisco small subunit α -helices via salt bridges and a hydrophobic**
854 **pocket. a-b**, Front (a) and side (b) views of the EPYC1₄₉₋₇₂ peptide (red) bound to the two α -
855 helices of the Rubisco small subunit (blue). **c-d**, Three pairs of residues form salt bridges
856 between the helix of the EPYC1₄₉₋₇₂ peptide and the helices on the Rubisco small subunit. Shown
857 are front (c) and side (d) views as in panel a and panel b. The distances from EPYC1 R64, R71
858 and E66 to Rubisco small subunit E24, D23 and R91 are 3.06 Å, 2.78 Å, and 2.79 Å,
859 respectively. **e-f**, A hydrophobic pocket is formed by three residues of the EPYC1₄₉₋₇₂ peptide
860 and three residues of helix B of the Rubisco small subunit. Shown are front (e) and side (f) views
861 as in panel a and panel b. **g**, Summary of the interactions observed between the EPYC1₄₉₋₇₂
862 peptide and the two α -helices of the Rubisco small subunit. Helices are highlighted; the residues
863 mediating interactions are bold; salt bridges are shown as dotted lines; residues contributing to
864 the hydrophobic pocket are shown in black.

865 **Fig. 4 | Interface residues on EPYC1 are required for binding and phase separation of**
866 **EPYC1 and Rubisco *in vitro*.** **a**, Rubisco binding to a peptide array representing every possible
867 single amino acid substitution for amino acids 56-71 of EPYC1. The binding signal was
868 normalized by the binding signal of the original sequence. **b**, The effect of mutating the central R
869 or K in each of EPYC1's Rubisco-binding regions on *in vitro* phase separation of EPYC1 with
870 Rubisco. Scale bar = 10 μm . For each condition, the experiment was performed twice
871 independently with similar results.

872 **Fig. 5 | Interface residues on Rubisco are required for yeast two-hybrid interactions**
873 **between EPYC1 and Rubisco, and for pyrenoid matrix formation *in vivo*.** **a**, The importance
874 of Rubisco small subunit residues for interaction with EPYC1 was tested by mutagenesis in a
875 yeast two-hybrid experiment. **b**, The Rubisco small subunit-less mutant T60 (*ΔrbcS*) was
876 transformed with wild-type, D23A/E24A or M87D/V94D Rubisco small subunits. Serial 1:10
877 dilutions of cell cultures were spotted on TP minimal medium and grown in air or 3% CO₂. **c-d**,
878 Representative electron micrographs of whole cells (c) and corresponding pyrenoids (d) of the
879 strains expressing wild-type, D23A/E24A, and M87D/V94D Rubisco small subunit. Dashes in
880 panel c indicate regions shown in panel d. Scale bars = 500 nm. At least 25 cells were imaged for
881 each strain; additional representative images are shown in Extended Data Fig. 10c.

882 **Fig. 6 | A model for matrix structure consistent with *in situ* Rubisco positions and**
883 **orientations. a**, The pyrenoid matrix was imaged by cryo-electron tomography⁵. An individual
884 slice through the three-dimensional volume is shown. Scale bar = 200 nm. **b**, The positions and
885 orientations of individual Rubisco holoenzymes (blue) were determined with high sensitivity and
886 specificity (97.5% positive identification) by template matching, subtomogram averaging, and
887 classification and then mapped back into the tomogram volume shown in panel a. The yellow
888 box indicates the region shown in panel c. Scale bar = 200 nm. **c**, The distances (yellow) between
889 the nearest EPYC1-binding sites (red) on neighboring Rubisco holoenzymes (blue) were
890 measured. The view is from inside the matrix; in some cases the nearest EPYC1 binding site is
891 on a Rubisco that is out of the field of view, causing some yellow lines to appear unconnected in
892 this image. Scale bar = 20 nm. The data shown in panels a-c are representative of the five
893 independent tomograms used for this study. **d**, Histogram showing the distances between the
894 nearest EPYC1 binding sites on neighboring Rubisco holoenzymes. The black line indicates the
895 median, and the yellow shading indicates 95% confidence interval based on data from five
896 independent tomograms. The estimated energy required for stretching a chain of 40 amino acids
897 a given distance is shown in blue. **e**, A 3D model illustrates how EPYC1 (red) could crosslink
898 multiple Rubisco holoenzymes (blue) to form the pyrenoid matrix. The conformations of the
899 intrinsically disordered linkers between EPYC1 binding sites were modeled hypothetically.

1
2
3

1. Extended Data

Figure #	Figure title One sentence only	Filename This should be the name the file is saved as when it is uploaded to our system. Please include the file extension. i.e.: <i>Smith_ED_Fig1.jpg</i>	Figure Legend If you are citing a reference for the first time in these legends, please include all new references in the Online Methods References section, and carry on the numbering from the main References section of the paper.
Extended Data Fig. 1	The EPYC1 peptides with the highest binding affinities to Rubisco were chosen for structural studies.	Extended_Data_Fig. 1-20200921.jpg	a, Diagram indicating the differences between the previously defined sequence repeats ¹⁰ and the newly defined sequence repeats on full-length EPYC1. b, To verify the Rubisco-binding regions on EPYC1, surface plasmon resonance (SPR) was used to measure the binding of EPYC1 peptides to Rubisco. Purified Rubisco was immobilized on a sensor surface, and the EPYC1 peptides in solution were injected over the surface. The binding activity was recorded in real time in a sensorgram. c, The peptides used in SPR experiments are shown aligned to the sequence as shown in Fig. 1. The Rubisco-binding signal from the SPR experiment of each peptide is shown after normalization to the peptide's molecular weight. EPYC1 ₄₉₋₇₂ (boxed in red) and EPYC1 ₁₀₆₋₁₃₅ (boxed in pink) were chosen for structural studies based on their reproducible high Rubisco binding signal. d, The Rubisco-binding response of the EPYC1 ₄₉₋₇₂ peptide at different concentrations was measured by SPR. e, The binding responses shown in (d) were fitted to estimate the K_D of EPYC1 ₄₉₋₇₂ peptide binding to Rubisco.
Extended Data Fig. 2	Single-particle cryo-EM data collection and image processing procedure.	Extended_Data_Fig. 2-20200919.jpg	a-c, Representative micrographs of the apo Rubisco sample (a), the Rubisco-EPYC1 ₄₉₋₇₂ complex (b) and the Rubisco-EPYC1 ₁₀₆₋₁₃₅ complex (c). Scale bars = 100 nm. d-f, Representative 2D class averages of the apo Rubisco sample (d), the Rubisco-EPYC1 ₄₉₋₇₂ complexes (e) and the Rubisco-

			EPYC1 ₁₀₆₋₁₃₅ complexes (f). g-i, Overview of the workflow for single-particle data processing for the apo Rubisco sample (g), the Rubisco-EPYC1 ₄₉₋₇₂ sample (h) and the Rubisco-EPYC1 ₁₀₆₋₁₃₅ sample (i). j-l, Local resolution estimation of the final refined apo Rubisco map (j), the final refined Rubisco-EPYC1 ₄₉₋₇₂ complex map (k) and the final refined Rubisco-EPYC1 ₁₀₆₋₁₃₅ complex map (l).
Extended Data Fig. 3	Cryo-EM analysis and resolution of apo Rubisco and Rubisco-EPYC1 peptide complexes in this study.	Extended_Data_Fig. 3-20200728.jpg	a-b, Representative cryo-EM density quality showing an α -helix of residues 214-232 in chain A (one of the Rubisco large subunits) (a) and a β -sheet of residues 36-43 in chain A (b) of the Rubisco-EPYC1 ₄₉₋₇₂ density map and structural model. The densities are shown as meshwork in gray. The backbones of the structural model are in ribbon representation, and side chains are shown in stick representation. c-d, Representative cryo-EM density quality showing water molecules as orange spheres. One water molecule between R312 and E136 on chain A is shown in panel c, and another water molecule between D137 and K316 on chain A is shown in panel d. e, Fourier shell correlation (FSC) curves of the final density maps of apo Rubisco and the Rubisco-EPYC1 peptide complexes.
Extended Data Fig. 4	Comparison of our EM structure of apo Rubisco and the published X-ray crystallography structure (1gk8) of Rubisco purified from <i>Chlamydomonas reinhardtii</i> ¹³ , and comparison of our EM structure of apo Rubisco and Rubisco bound with EPYC1 ₄₉₋₇₂ peptide.	Extended_Data_Fig. 4-20200527.jpg	a, Comparison of the structure of the small subunit of apo Rubisco obtained here by EM with 1gk8. The EM structure has additional C-terminus density past residue 126, circled by a red dashed line. b, Comparison of our two EM structures of the small subunit: from apo Rubisco and from EPYC1 ₄₉₋₇₂ peptide-bound Rubisco. c, Comparison of the structure of the large subunit of apo Rubisco obtained here by EM with 1gk8. The three major differences found between the X-ray structure and the EM structure of the large subunit are circled with red dashed lines. d, Comparison of our two EM structures of the large subunit: from apo Rubisco and from EPYC1 ₄₉₋₇₂ peptide-bound Rubisco. The major difference found between the EPYC1 ₄₉₋₇₂ peptide-bound structure and the apo EM structure was the loop between K175 and L180 of the large

			subunit, which is shown circled by a red dashed line.
Extended Data Fig. 5	Additional residues may contribute to the interaction between EPYC1 and Rubisco.	Extended_Data_Fig. 5-20200804-4.jpg	Our Rubisco-EPYC1 ₄₉₋₇₂ peptide structure suggests that R56 of the EPYC1 ₄₉₋₇₂ peptide may interact with D31 of the Rubisco small subunit and E433 of the Rubisco large subunit (the atoms of the backbone of E433 are also shown to display the possible interaction). R51 of the EPYC1 ₄₉₋₇₂ peptide may form a salt bridge with Y32 of the Rubisco small subunit. Residues S57 and V58 of the EPYC1 ₄₉₋₇₂ peptide are close to D31 in the structure, which may explain why replacing either of these residues with a negatively charged residue disrupts binding (Fig. 4a).
Extended Data Fig. 6	The EPYC1 ₁₀₆₋₁₃₅ peptide binds to Rubisco small subunit α -helices via salt bridges and a hydrophobic pocket in a similar manner to the EPYC1 ₄₉₋₇₂ peptide.	Extended_Data_Fig. 6-20200730.jpg	a, The EPYC1 ₁₀₆₋₁₃₅ peptide represents the second, third and fourth Rubisco-binding regions of EPYC1 indicated by pink lines and dash line (the peptide is a perfect match to the second and fourth Rubisco-binding regions, and there is a one-amino acid difference between the peptide and the third repeat). b-c, Side view (b) and top view (c) of the density map of the EPYC1 ₁₀₆₋₁₃₅ peptide-Rubisco complex. Dashes in panel b indicate regions shown in panels d-i. d-e, Front (d) and side (e) views of the EPYC1 ₁₀₆₋₁₃₅ peptide (red) bound to the two α -helices of the Rubisco small subunit (blue). f-g, Three pairs of residues form salt bridges between the helix of the EPYC1 ₁₀₆₋₁₃₅ peptide and the helices on the Rubisco small subunit. Shown are front (f) and side (g) views as in panel d and panel e. The distances from EPYC1 K127, R134 and E129 to Rubisco small subunit E24, D23 and R91 are 2.96 Å, 3.17 Å, and 2.68 Å, respectively. h-i, A hydrophobic pocket is formed by three residues of the EPYC1 ₁₀₆₋₁₃₅ peptide and three residues of helix B of the Rubisco small subunit. Shown are front (h) and side (i) views as in panel d and panel e. j, Summary of the interactions observed between the EPYC1 ₁₀₆₋₁₃₅ peptide and the two α -helices of the Rubisco small subunit. Helices are highlighted; the residues mediating interactions are bold; salt bridges are shown as dotted lines; residues contributing to the

			hydrophobic pocket are shown in black. k, Color keys used in this figure.
Extended Data Fig. 7	Surface plasmon resonance analysis of binding of point mutants of EPYC1 ₅₅₋₇₂ to Rubisco.	Extended_Data_Fig. 7-20200722.jpg	The wild-type (WT) peptide or peptides with the indicated mutations were synthesized, and their Rubisco-binding signal was measured by surface plasmon resonance.
Extended Data Fig. 8	Interface residues on EPYC1 identified by cryo-EM are important for binding and phase separation of EPYC1 and Rubisco.	Extended_Data_Fig. 8-20200722.jpg	a, SDS-PAGE analysis of purified proteins used for <i>in vitro</i> phase separation experiments. WT = wild-type EPYC1; R/K = EPYC1 ^{R64A/K127A/K187A/K248A/R314} . b-c, A droplet sedimentation assay was used as a readout of phase separation complementary to the microscopy analyses shown in Fig. 4b. Proteins at indicated concentrations were mixed and incubated for 10 minutes, then condensates were pelleted by centrifugation. Supernatant (S) and pellet (P) fractions were run on a denaturing gel. The negative controls with no Rubisco or with no EPYC1 are shown in (b), and the wild-type Rubisco with wild-type EPYC1 or mutant EPYC1 are shown in (c). Data shown here are representative of two independent replicates.
Extended Data Fig. 9	Yeast two-hybrid assays of interactions between EPYC1 and wild-type or mutated Rubisco small subunit.	Extended_Data_Fig. 9-20200803.jpg	Colonies are shown after 3 days growth on plates. A subset of the data shown in this figure is shown in Fig. 5a.
Extended Data Fig. 10	Selection of the Rubisco small subunit mutant strains for phenotype analysis.	Extended_Data_Fig. 10-20200920.jpg	a, The Rubisco small subunit-less mutant T60 ($\Delta rbcS$) was transformed with DNA encoding wild-type and mutant Rubisco small subunits (RBCS) to produce candidate transformants with the genotypes $\Delta rbcS;RBCS^{WT}$, $\Delta rbcS;RBCS^{D23A/E24A}$, and $\Delta rbcS;RBCS^{M87D/V94D}$. Total protein extracts for three strains from each transformation were separated on a polyacrylamide gel. b, The gel shown in panel a was probed by Western blot using a polyclonal antibody mixture that detects both large and small Rubisco subunits. The experiments shown in panel a and b were performed once for selecting the candidate transformants with the

			<p>highest RBCS expression level from each genotype, in case any phenotype may be caused by low expression level of Rubisco. Selected strains are indicated by an arrow below the lanes and were used for the subsequent phenotypic analyses shown in Fig. 5 and panel c. c, Additional representative TEM images of whole cells of the strains expressing wild-type, D23A/E24A, and M87D/V94D Rubisco small subunit. Scale bar = 500 nm. For each strain, at least 25 images (one image for one cell) were taken and showing similar results.</p>
--	--	--	--

4 **2. Supplementary Information:**

5

6 **A. Flat Files**

7

8

Item	Present?	Filename This should be the name the file is saved as when it is uploaded to our system, and should include the file extension. The extension must be .pdf	A brief, numerical description of file contents. i.e.: <i>Supplementary Figures 1-4, Supplementary Discussion, and Supplementary Tables 1-4.</i>
Supplementary Information	Yes	Supplementary_Table 1-2_20201016.pdf	Supplementary Tables 1-2
Reporting Summary	Yes	200923_nr-reporting-summary_SH.pdf	

9

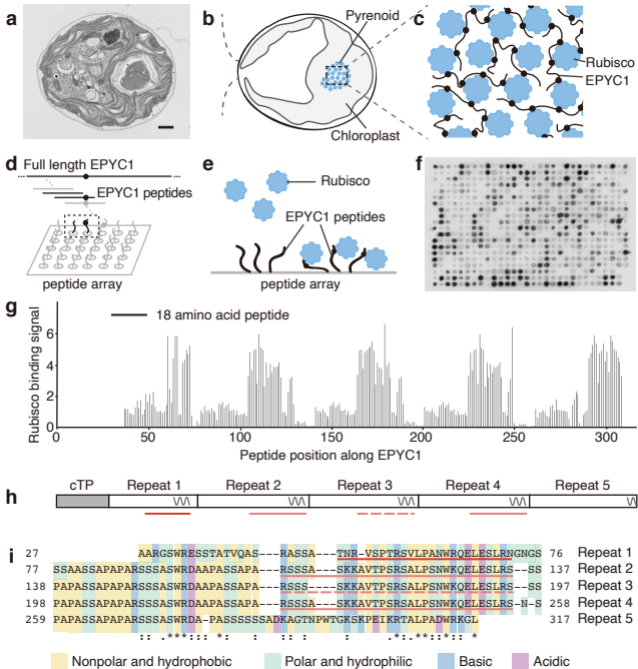
10

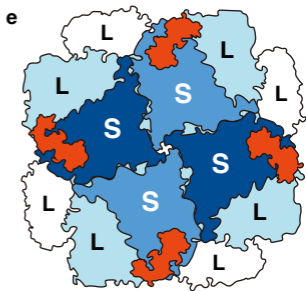
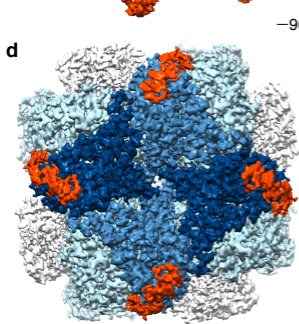
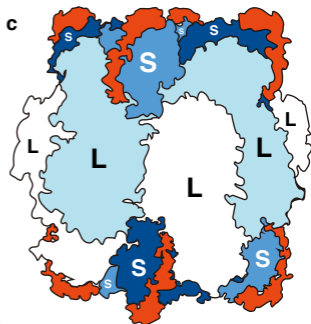
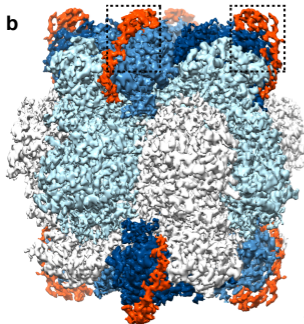
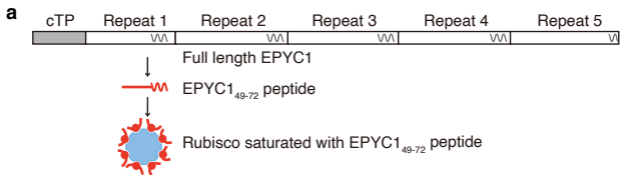
11 **B. Additional Supplementary Files**

12

13

Type	Number If there are multiple files of the same type this should be the numerical indicator. i.e. "1" for Video 1, "2" for Video 2, etc.	Filename This should be the name the file is saved as when it is uploaded to our system, and should include the file extension. i.e.: <i>Smith_Supplementary_Video_1.mov</i>	Legend or Descriptive Caption Describe the contents of the file
Supplementary Table	1	Supplementary_Table_3-5_20201016.xlsx	Supplementary Tables 3-5

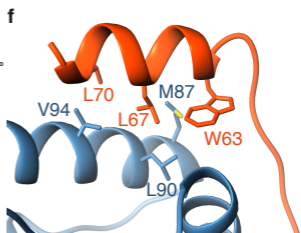
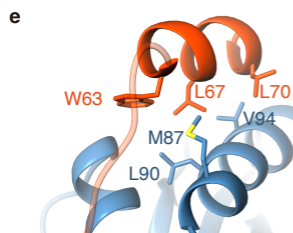
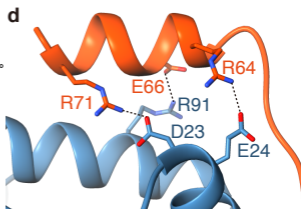
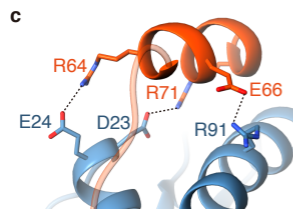
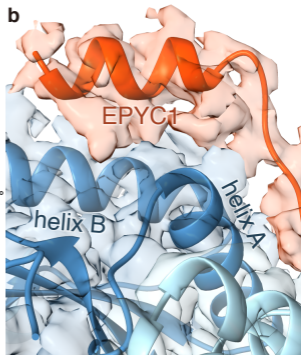
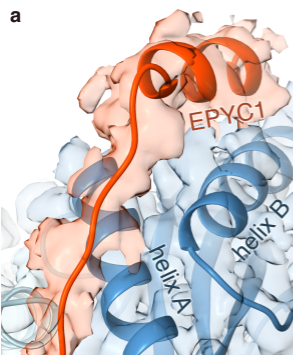


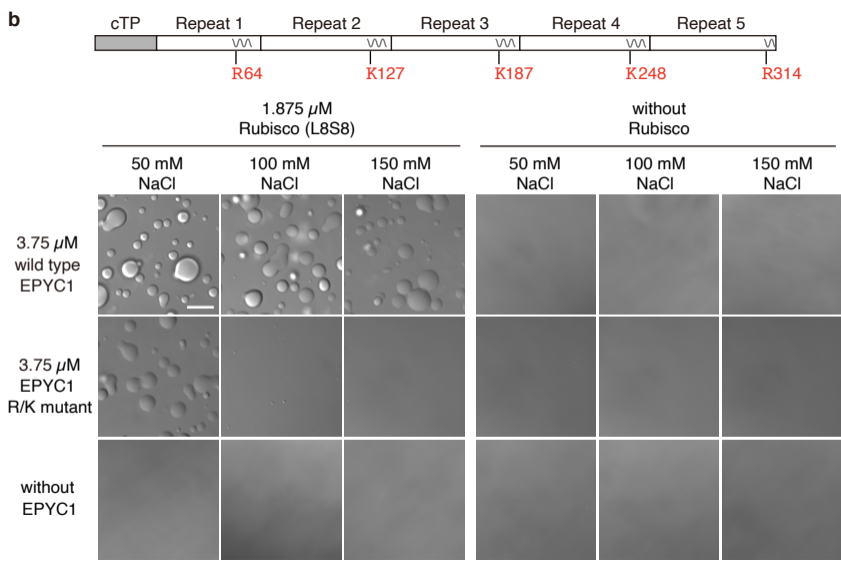
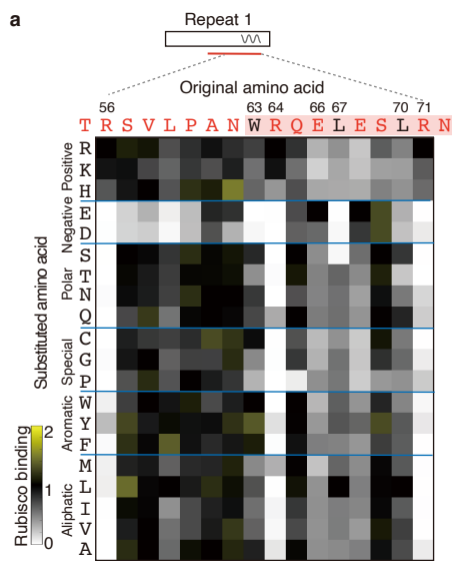


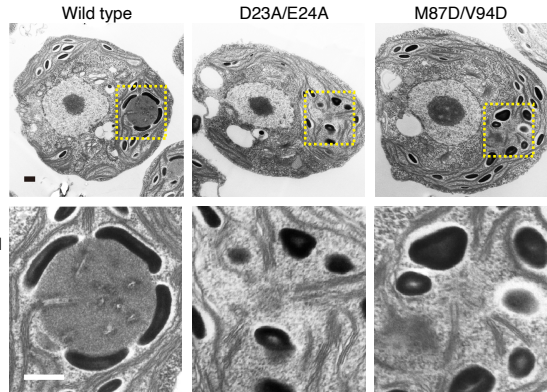
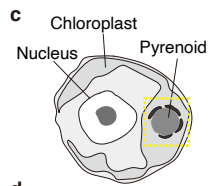
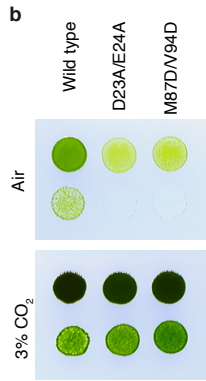
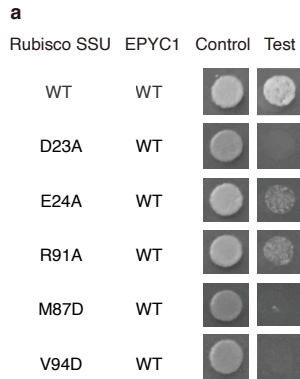
□ Rubisco large subunit

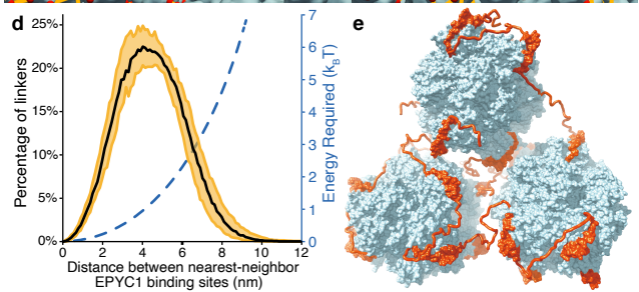
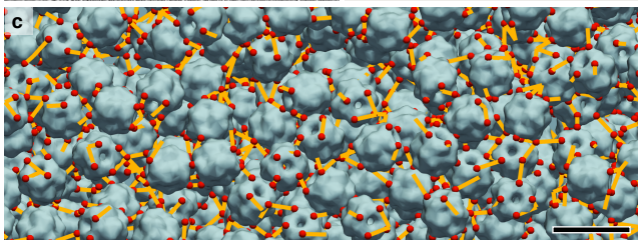
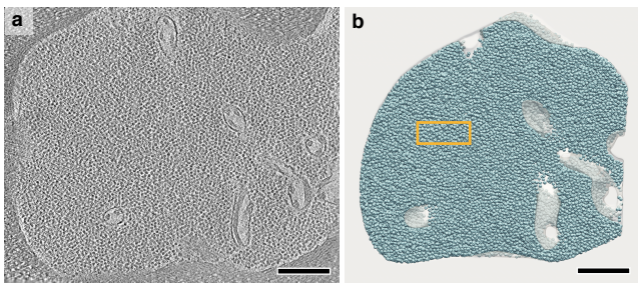
■ Rubisco small subunit

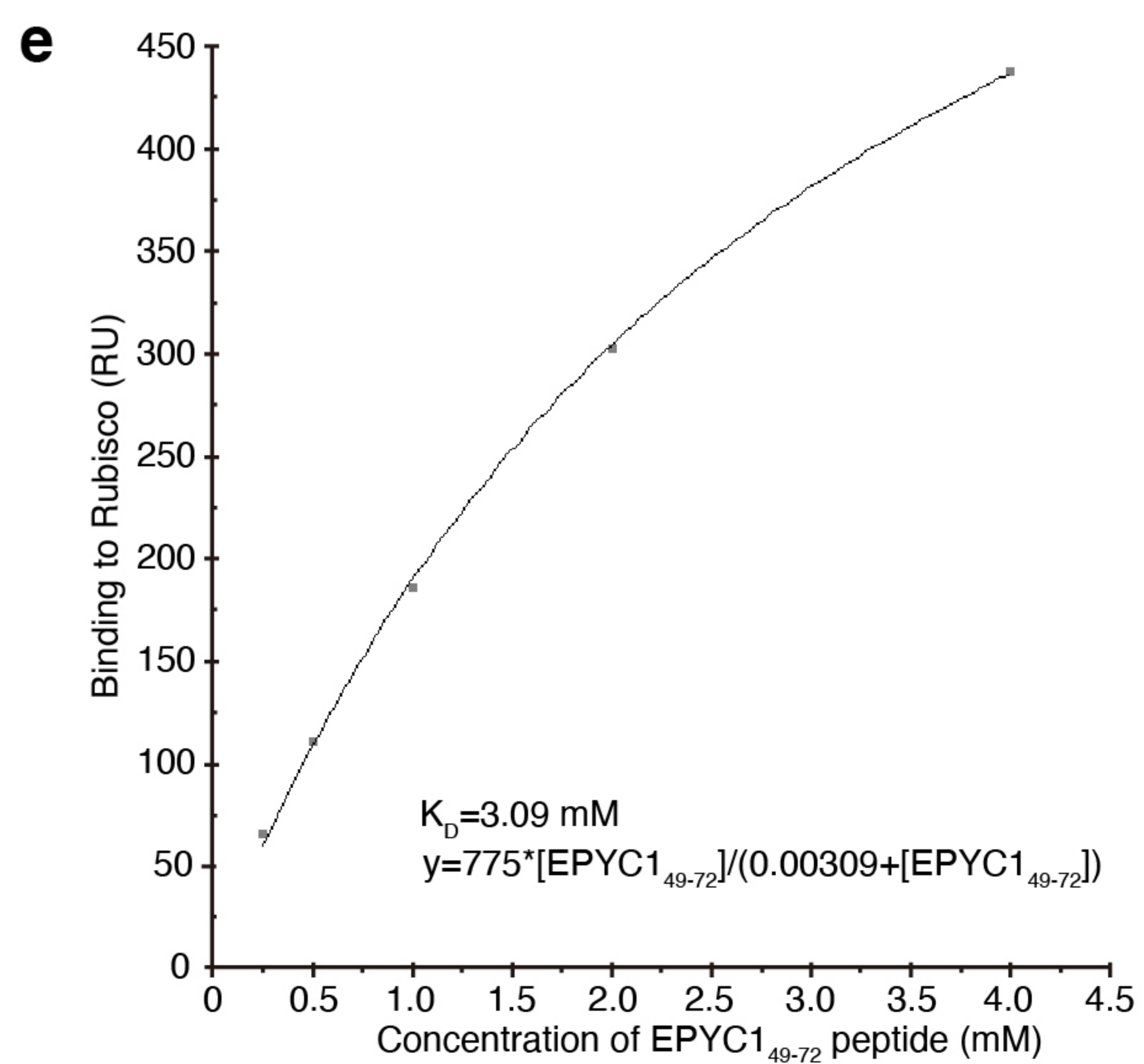
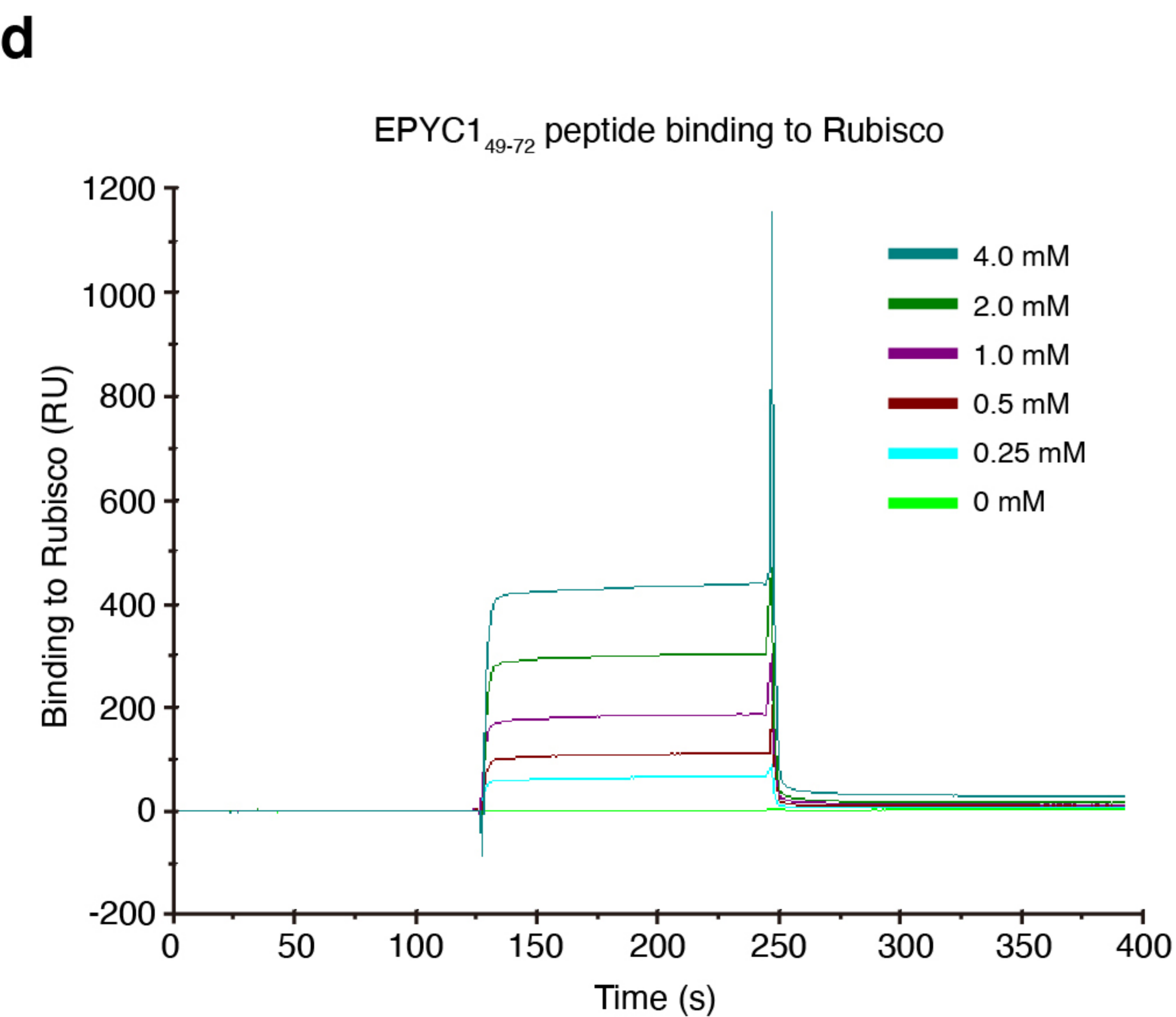
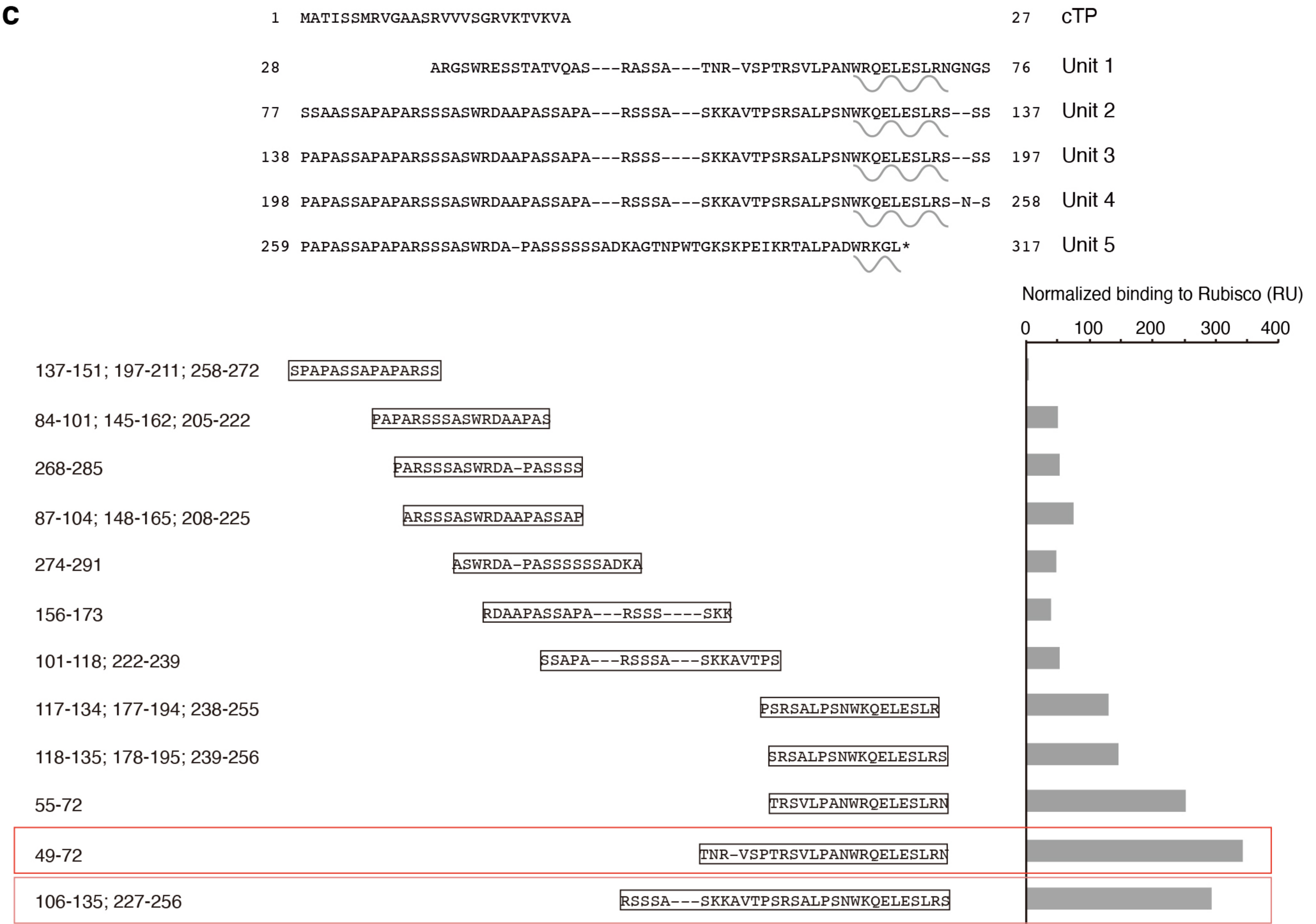
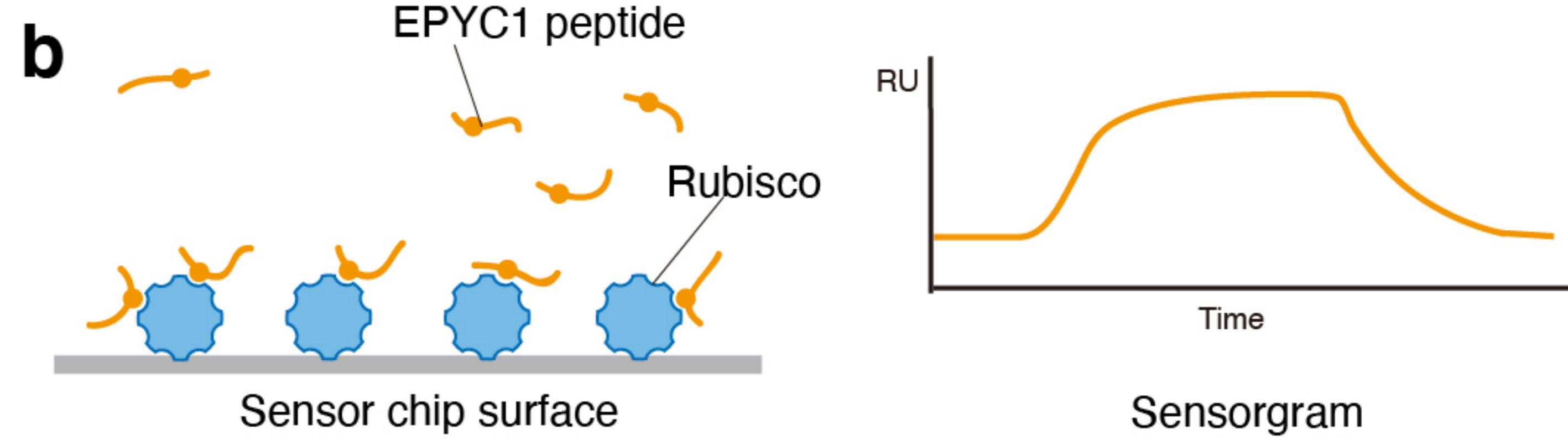
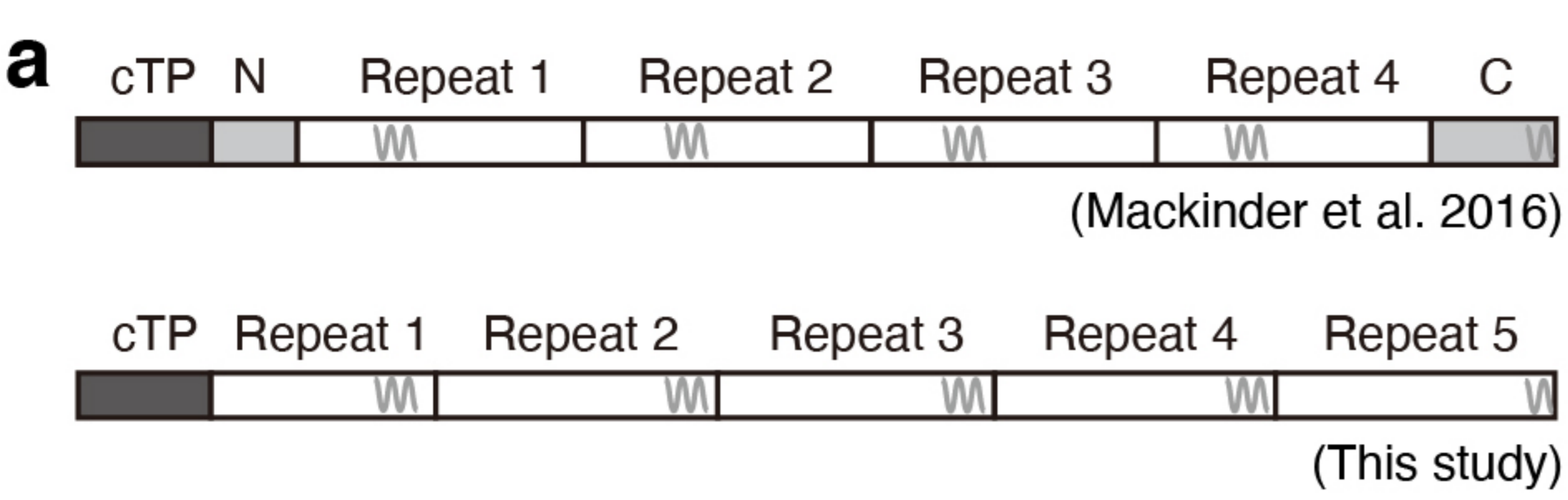
■ EPYC1 peptide



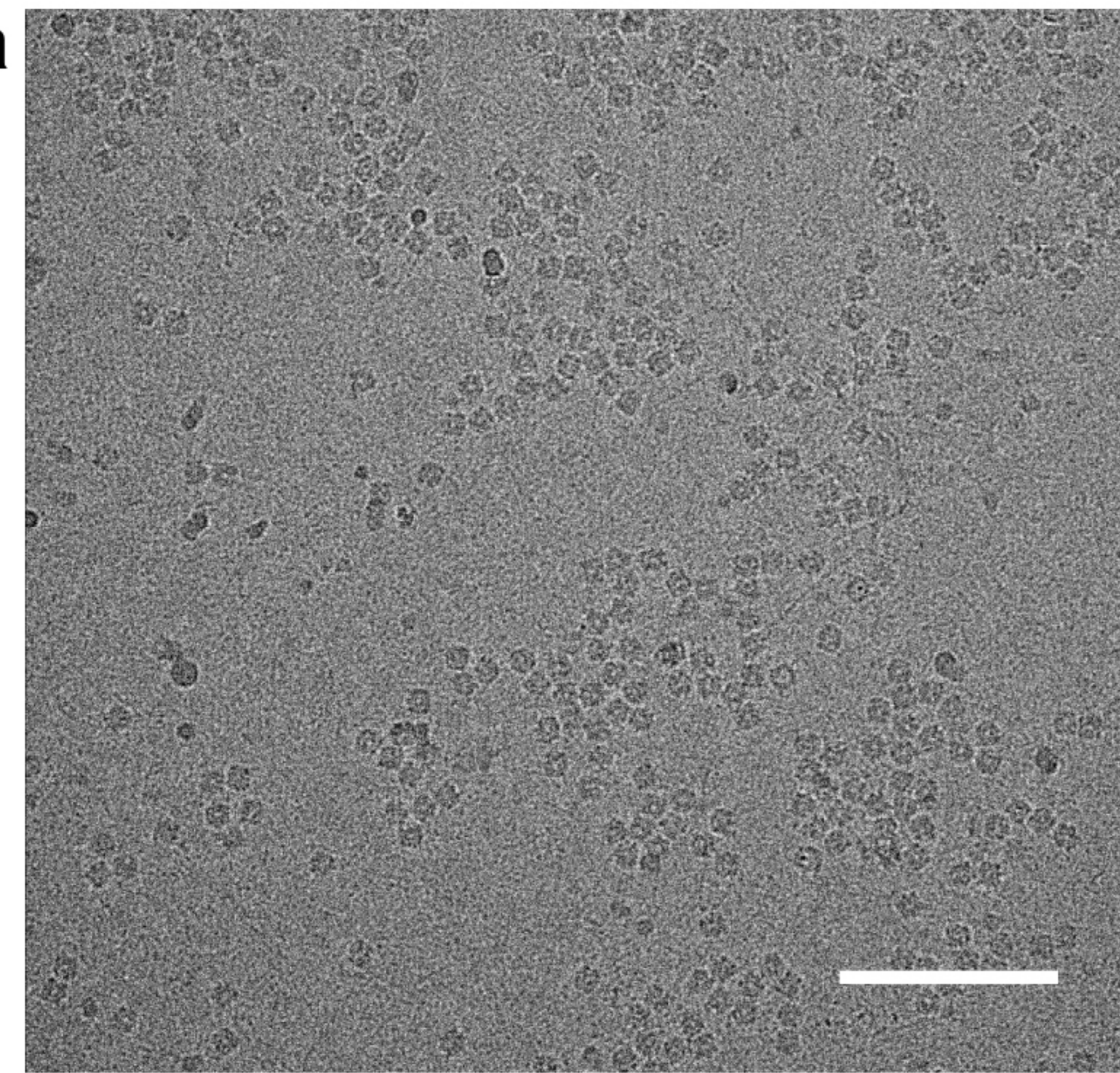




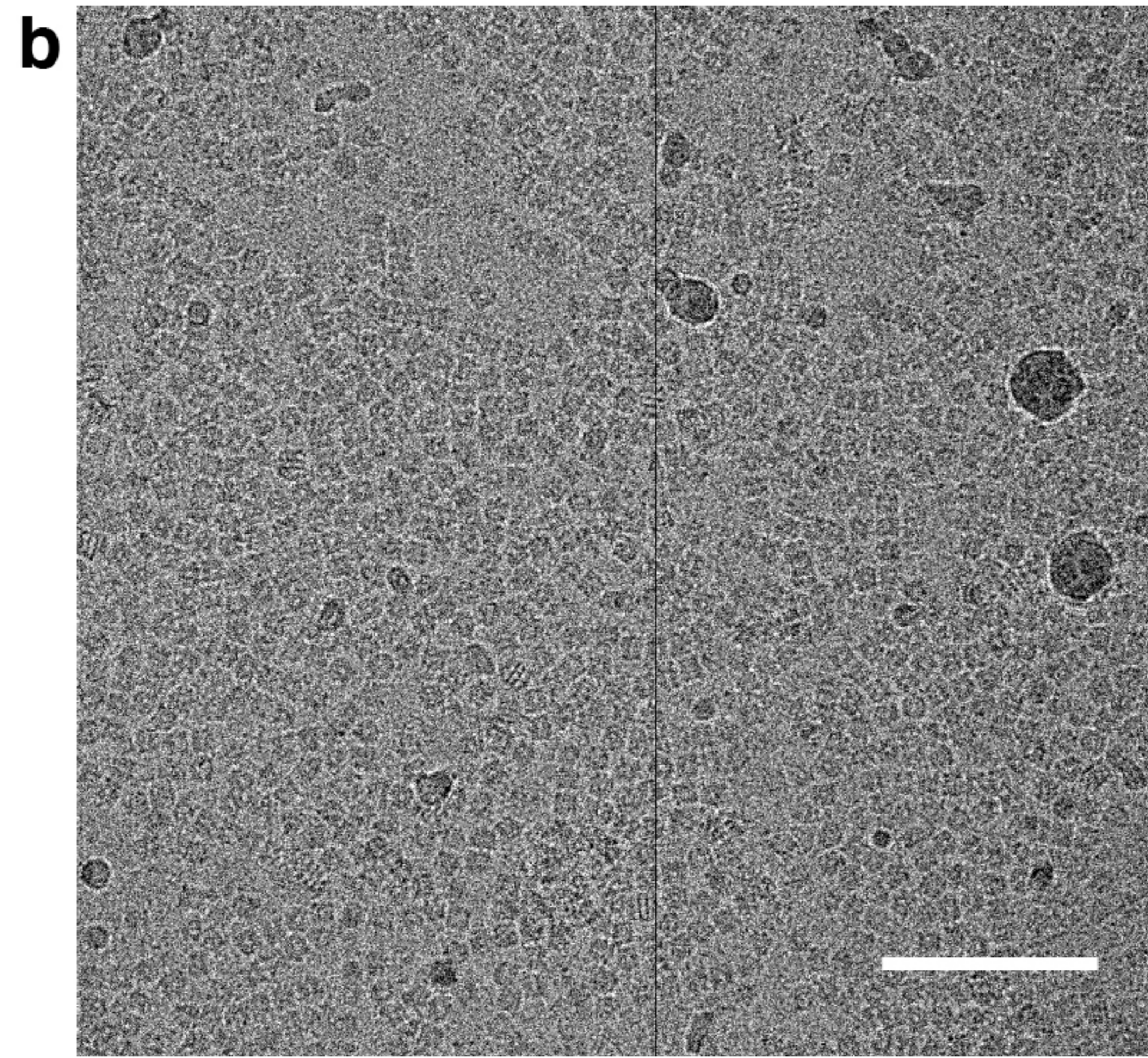




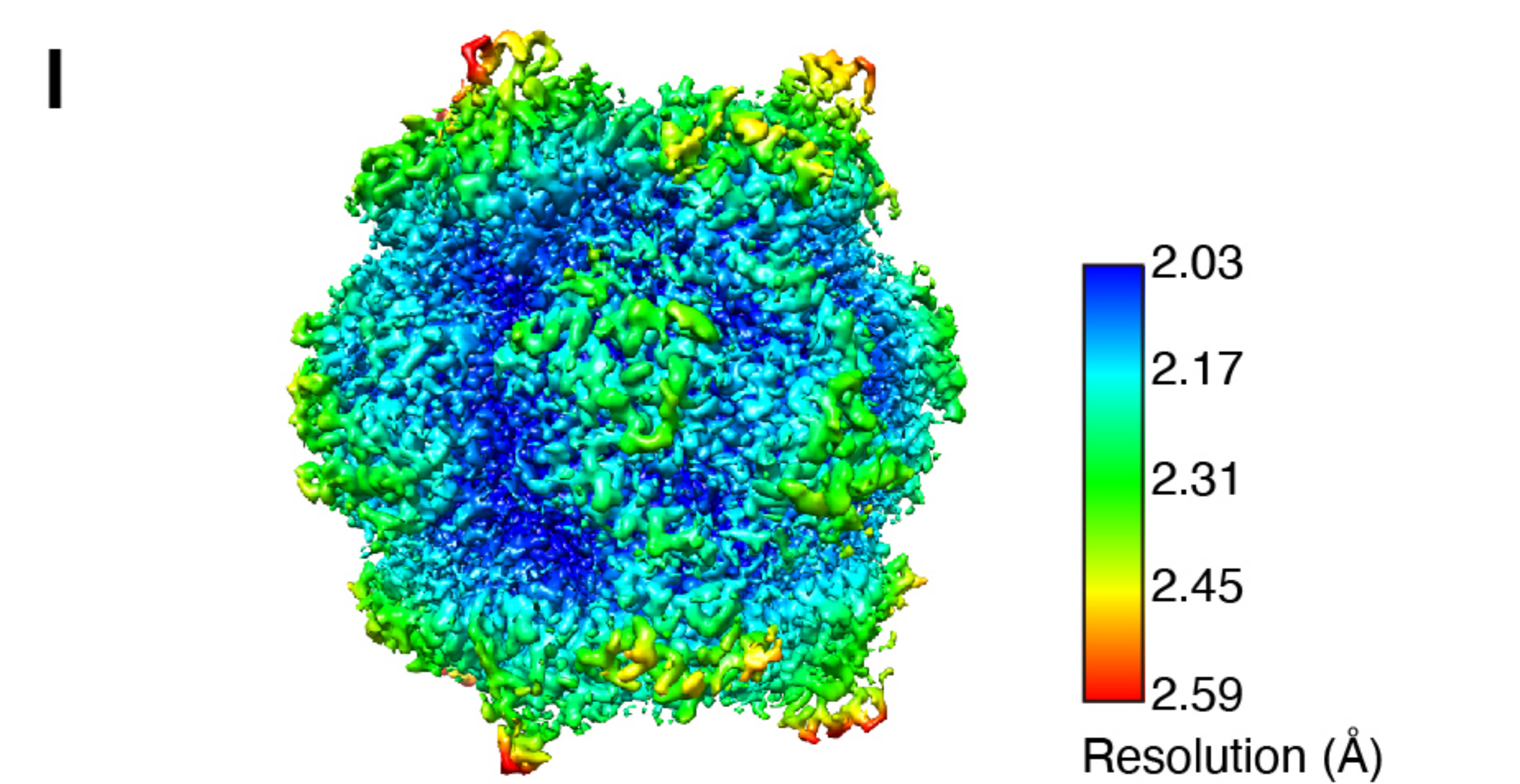
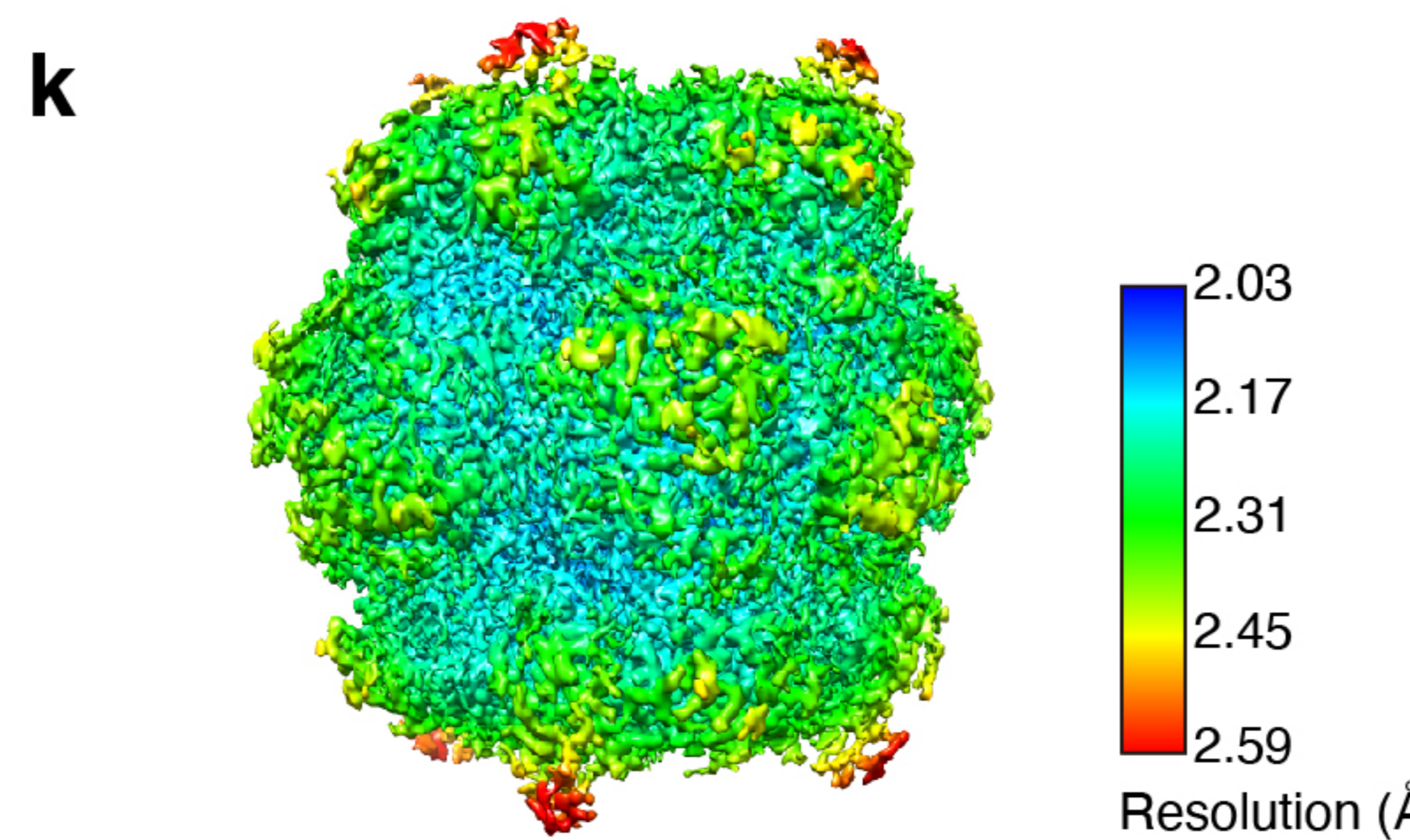
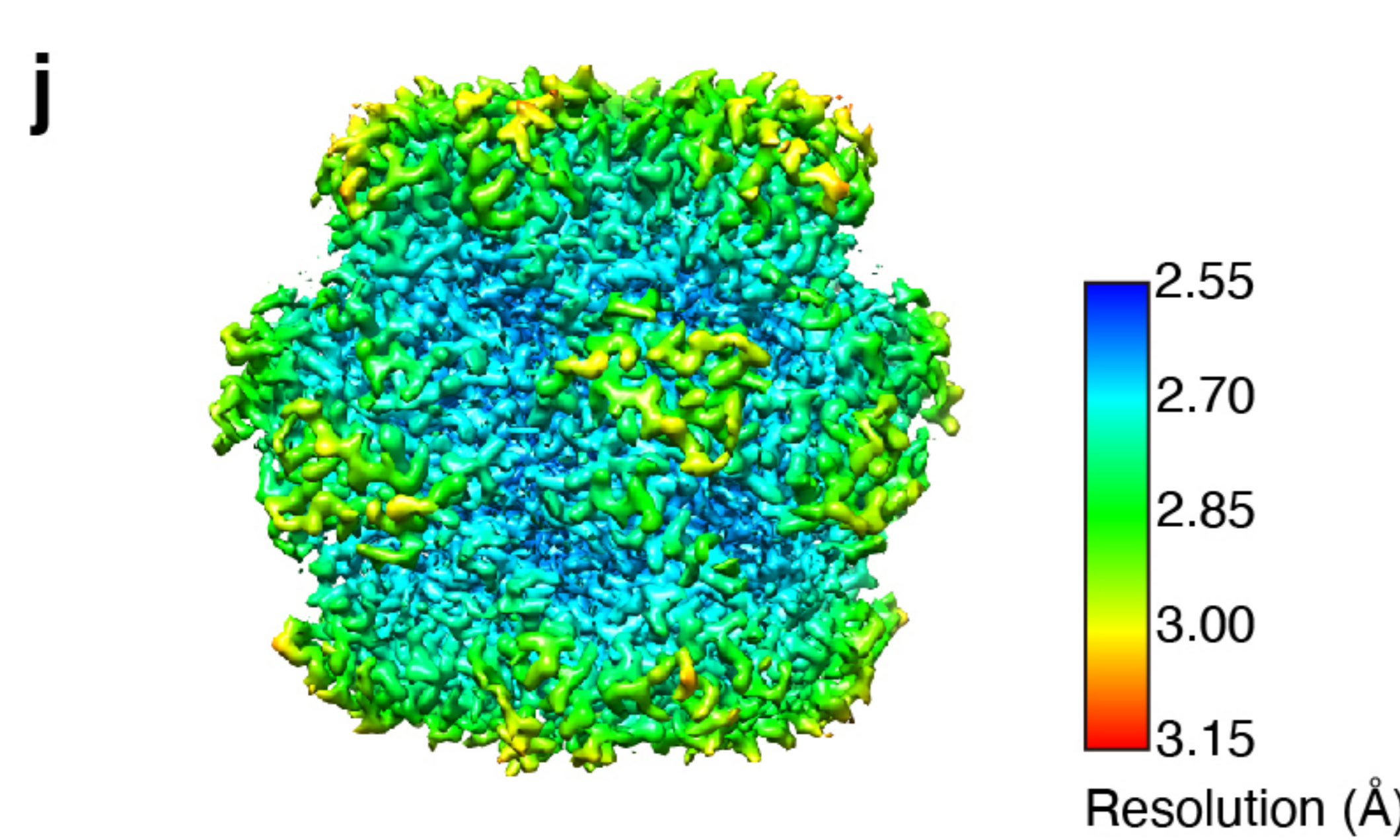
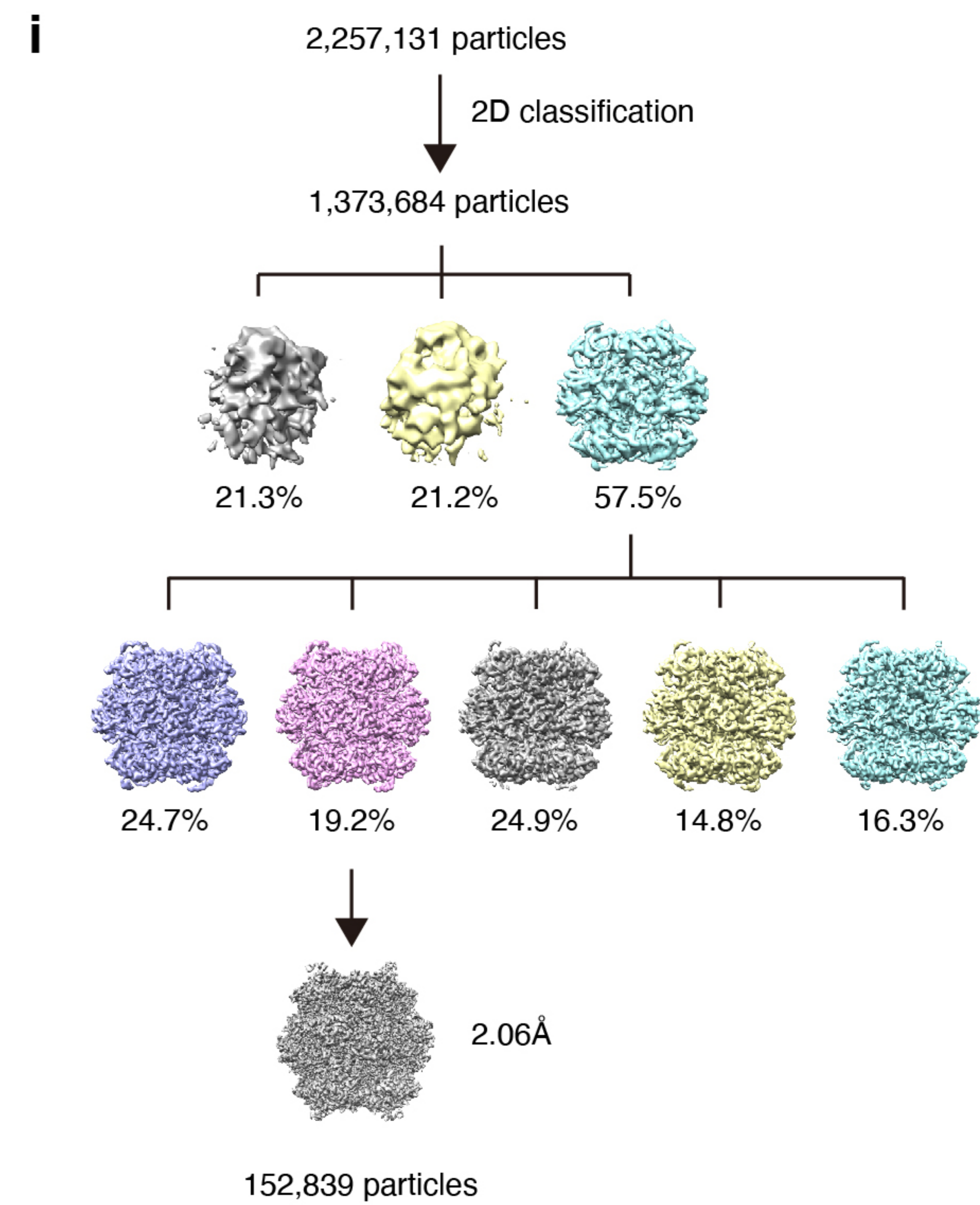
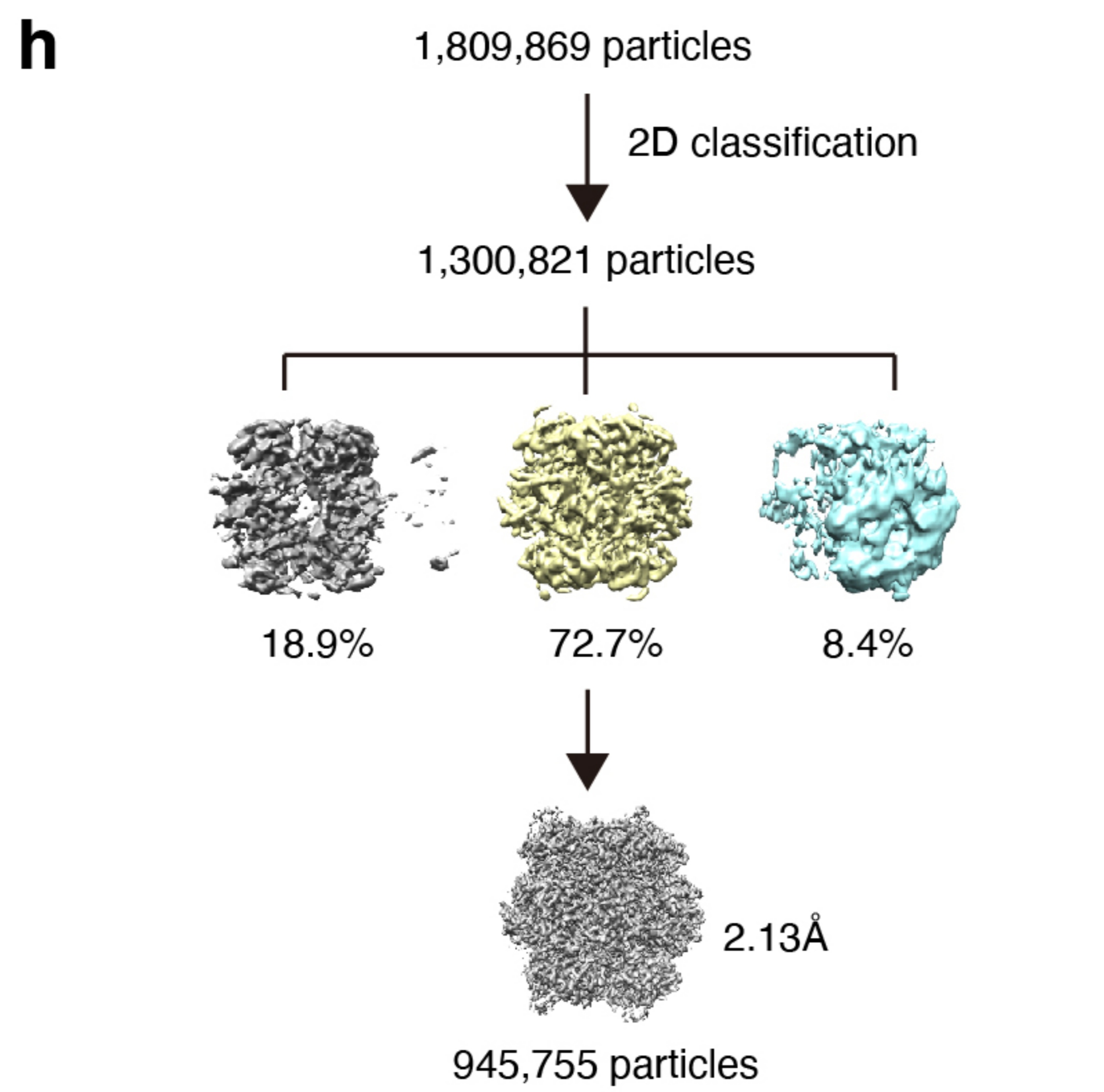
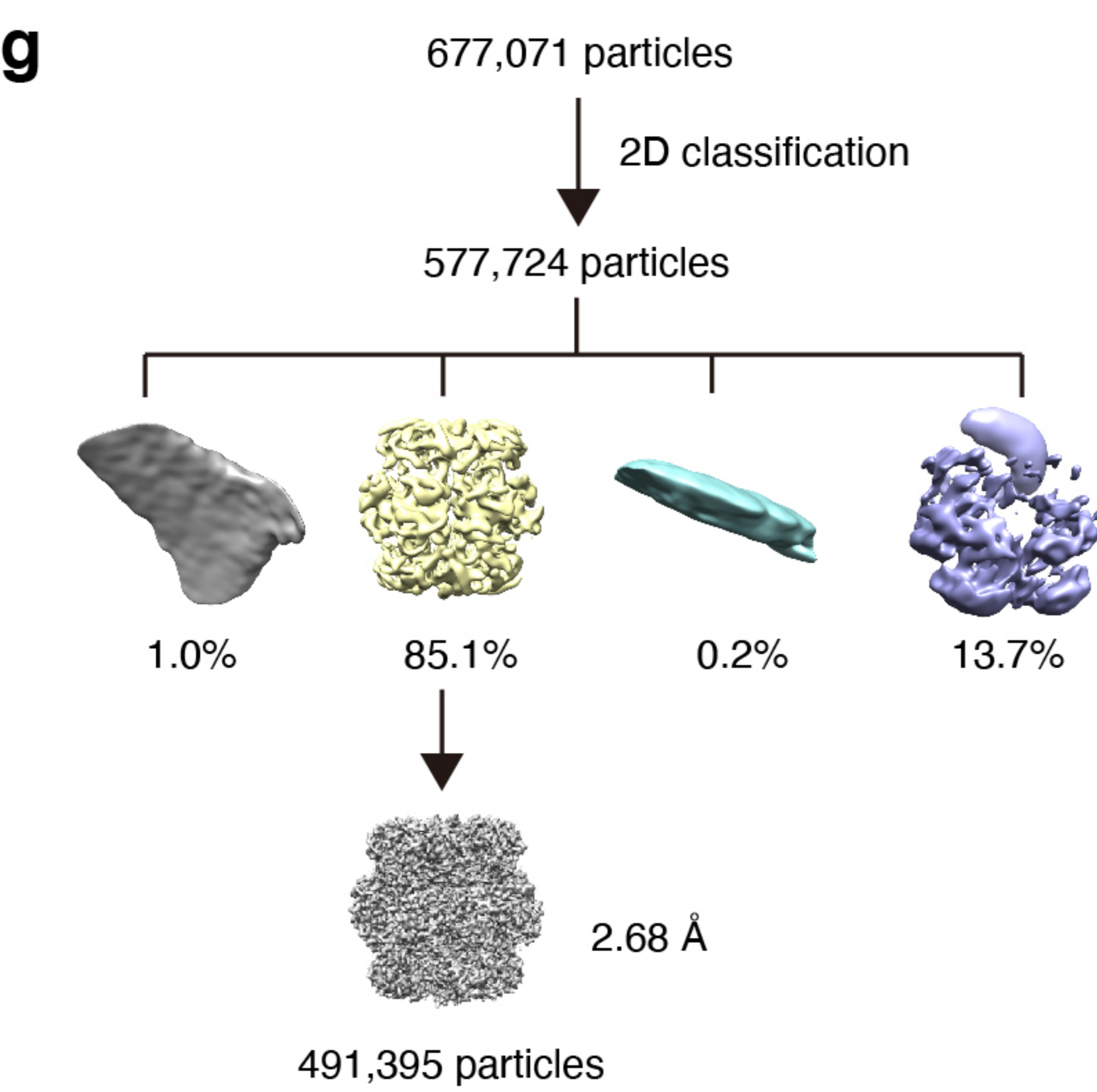
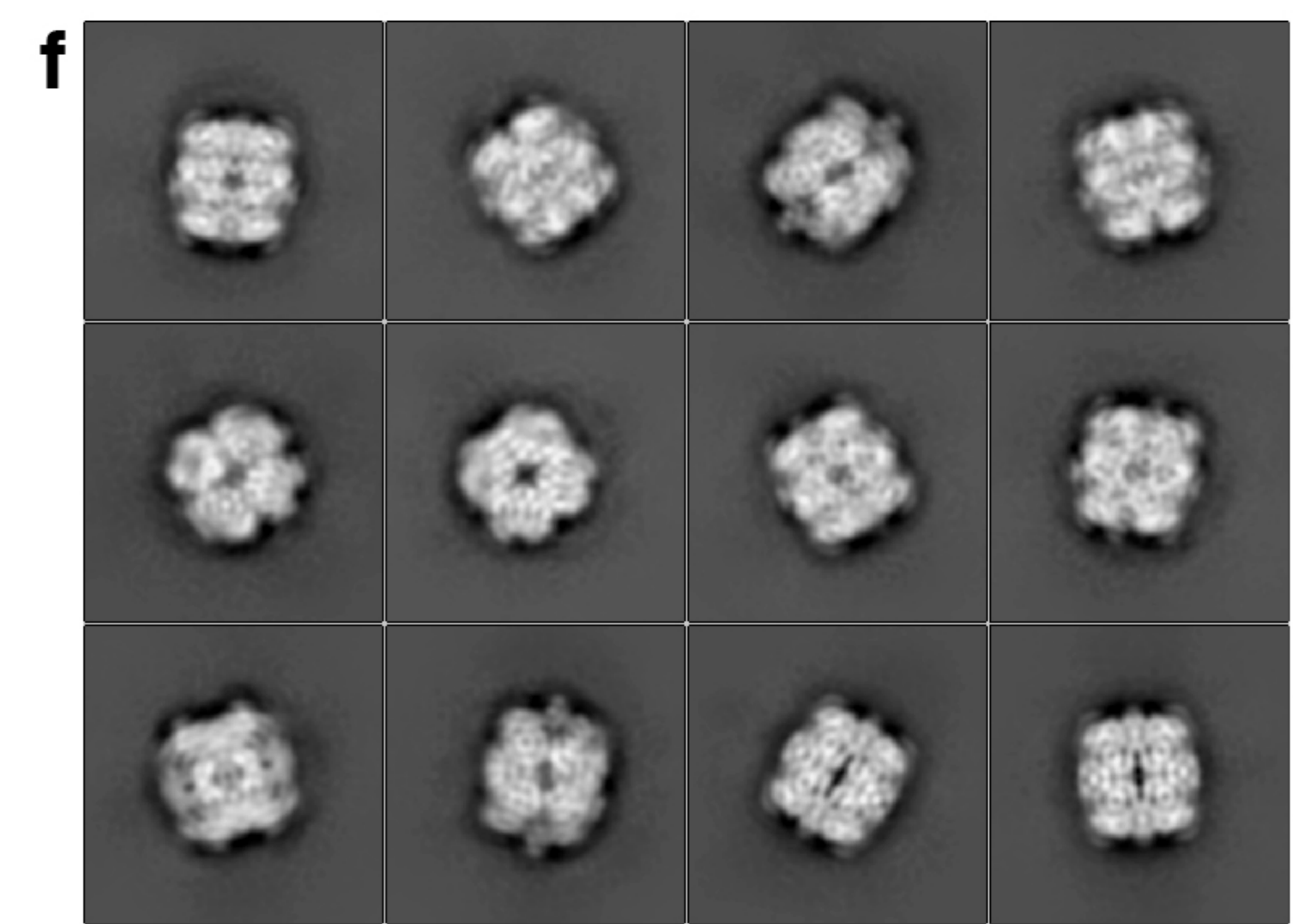
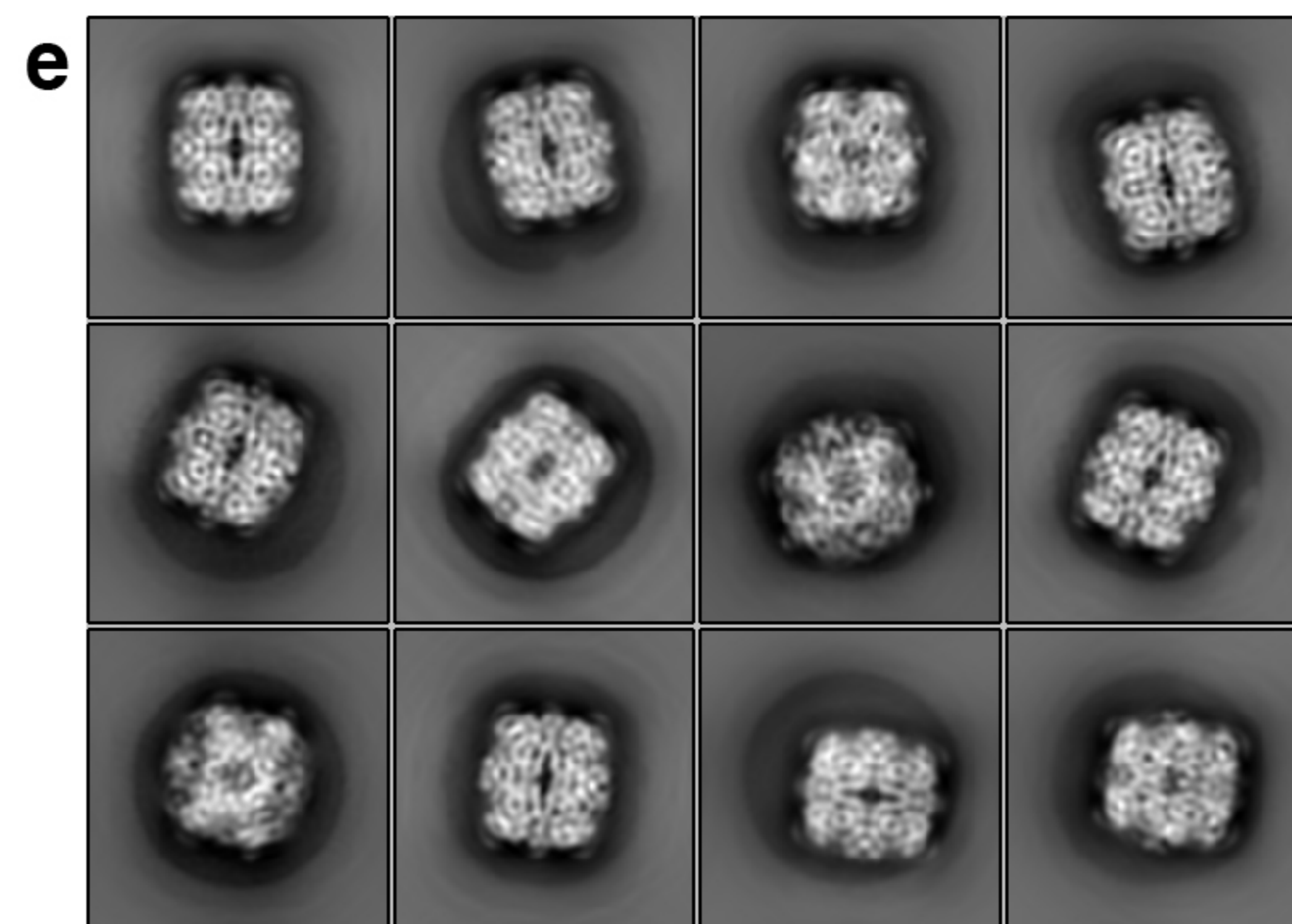
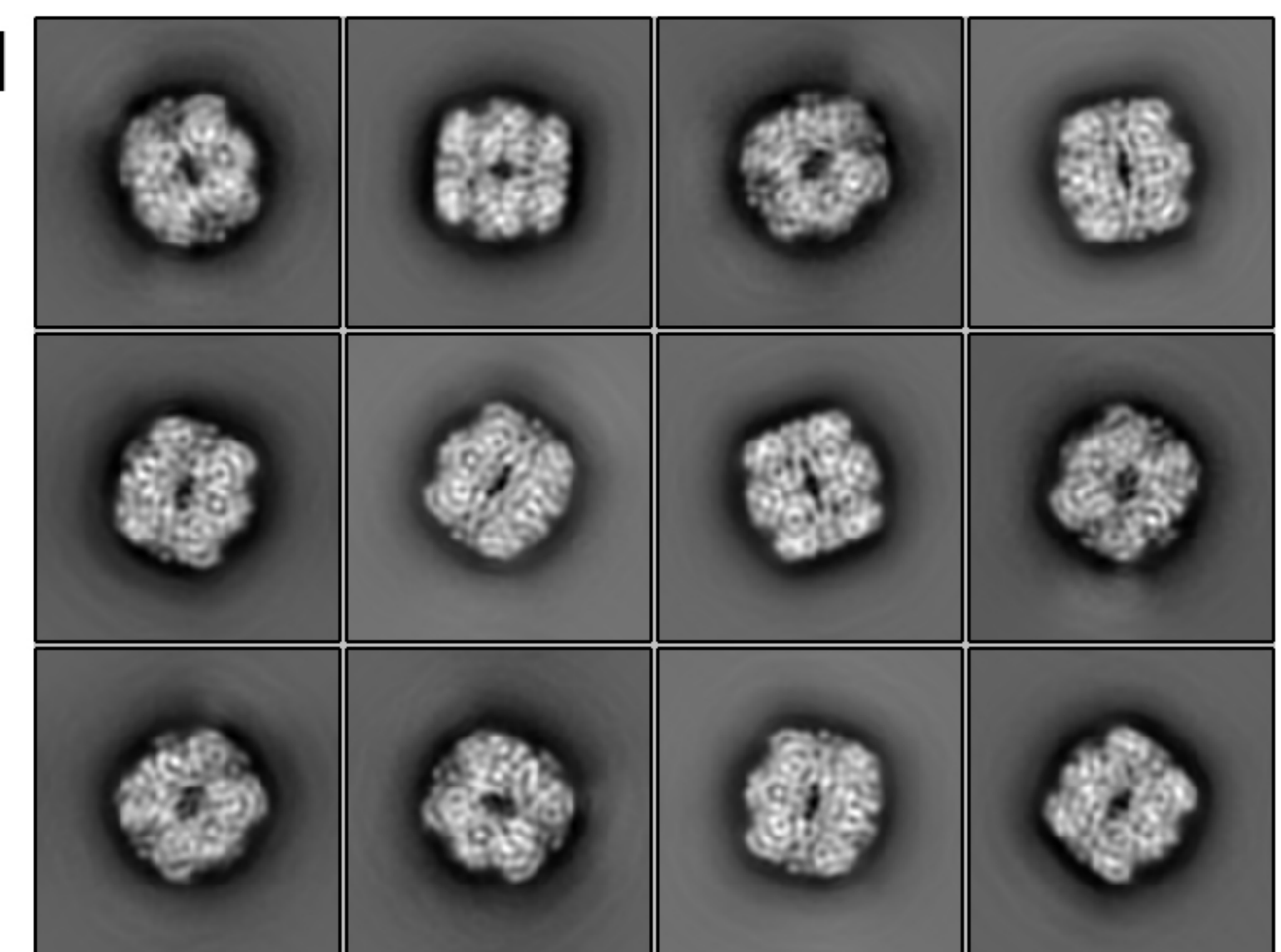
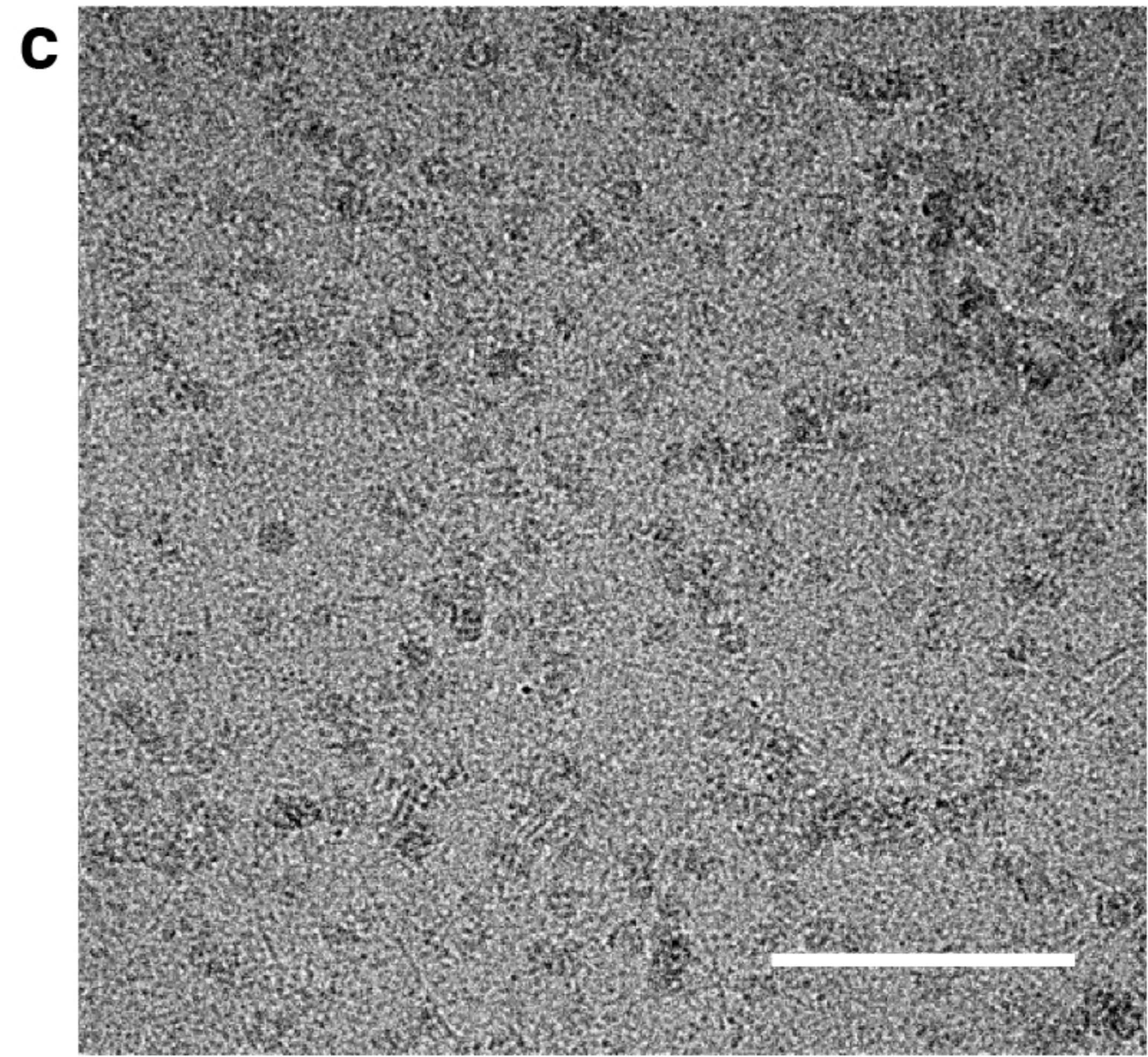
Apo Rubisco
(1,834 micrographs)

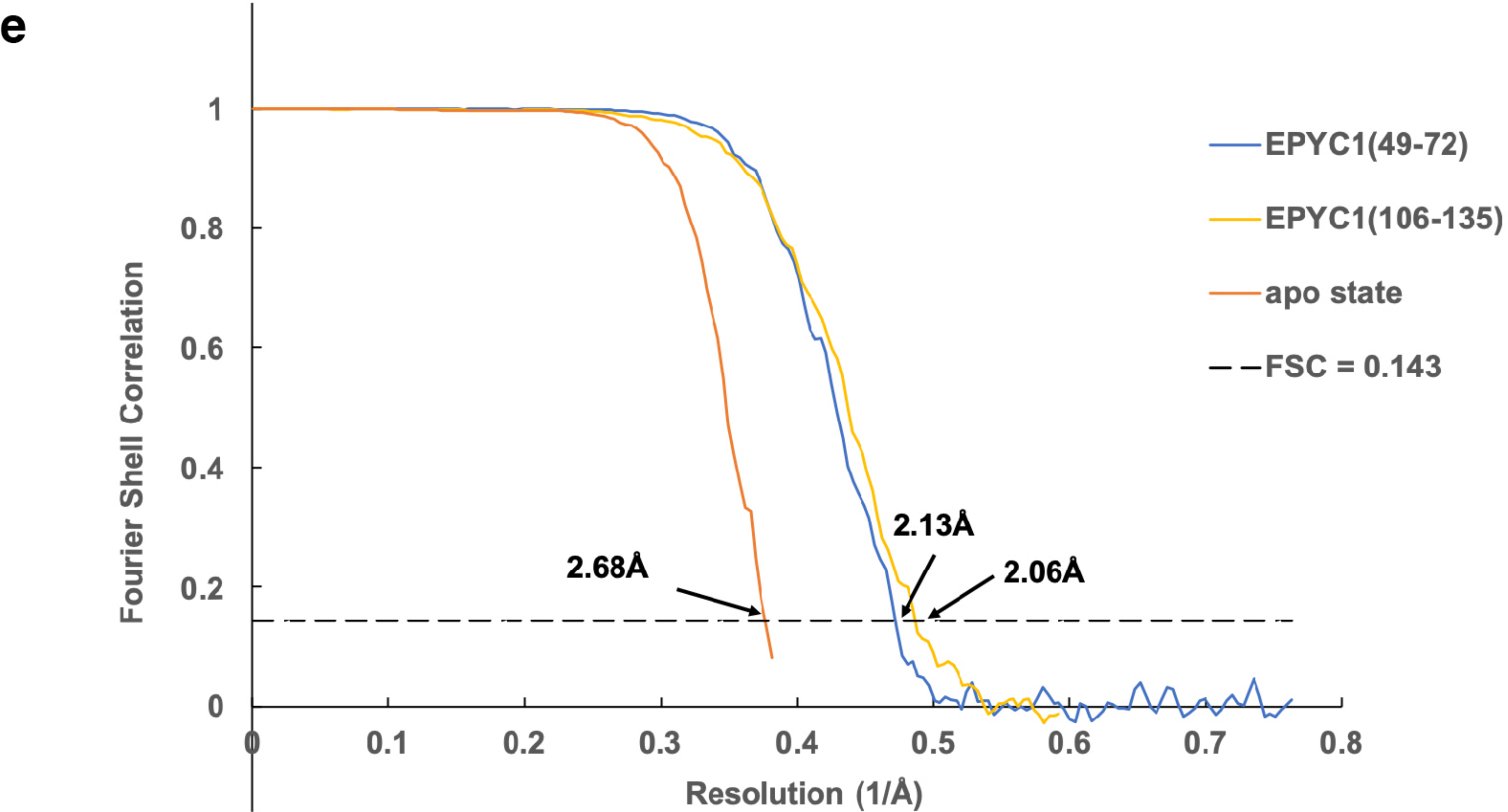
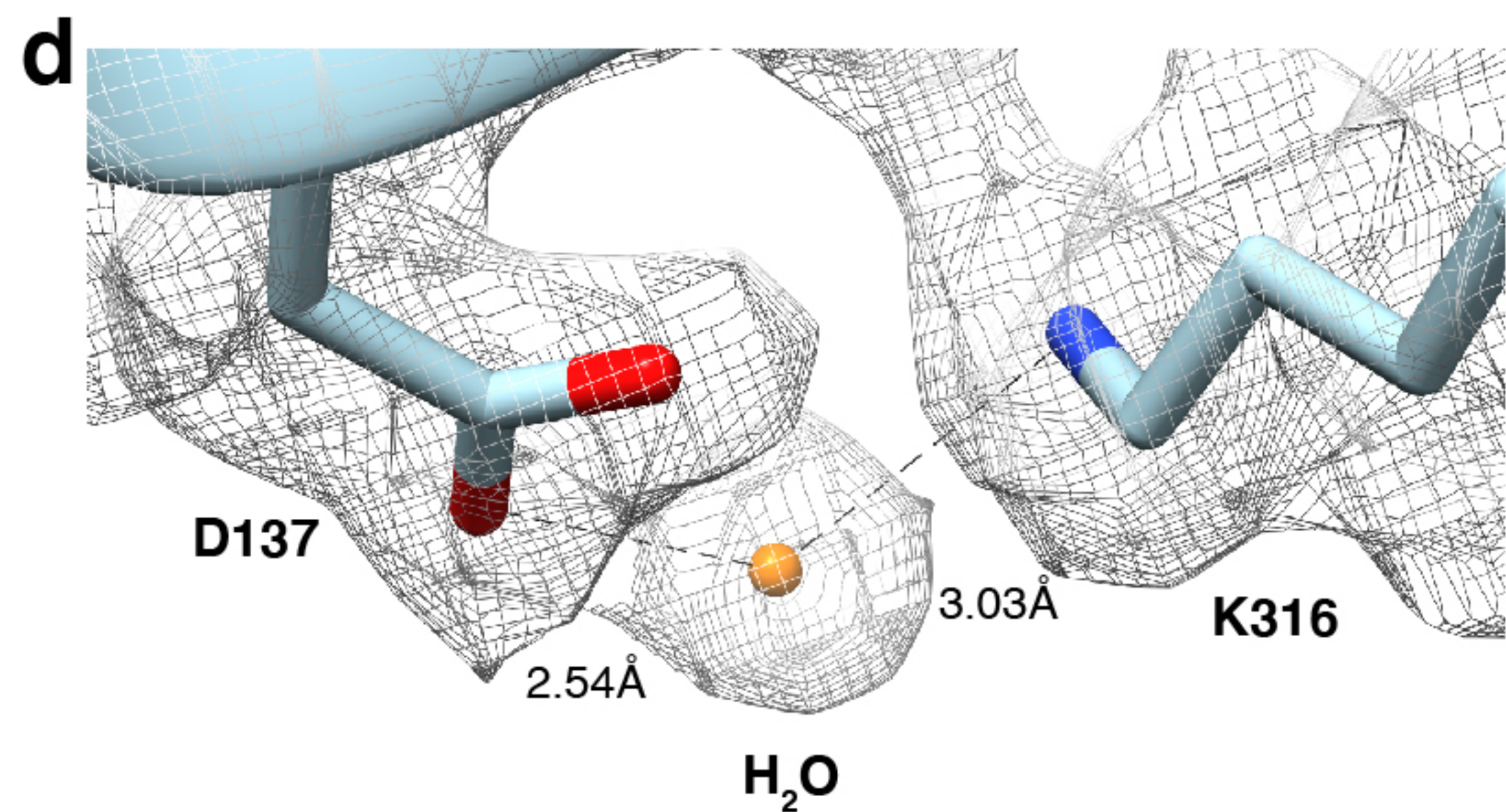
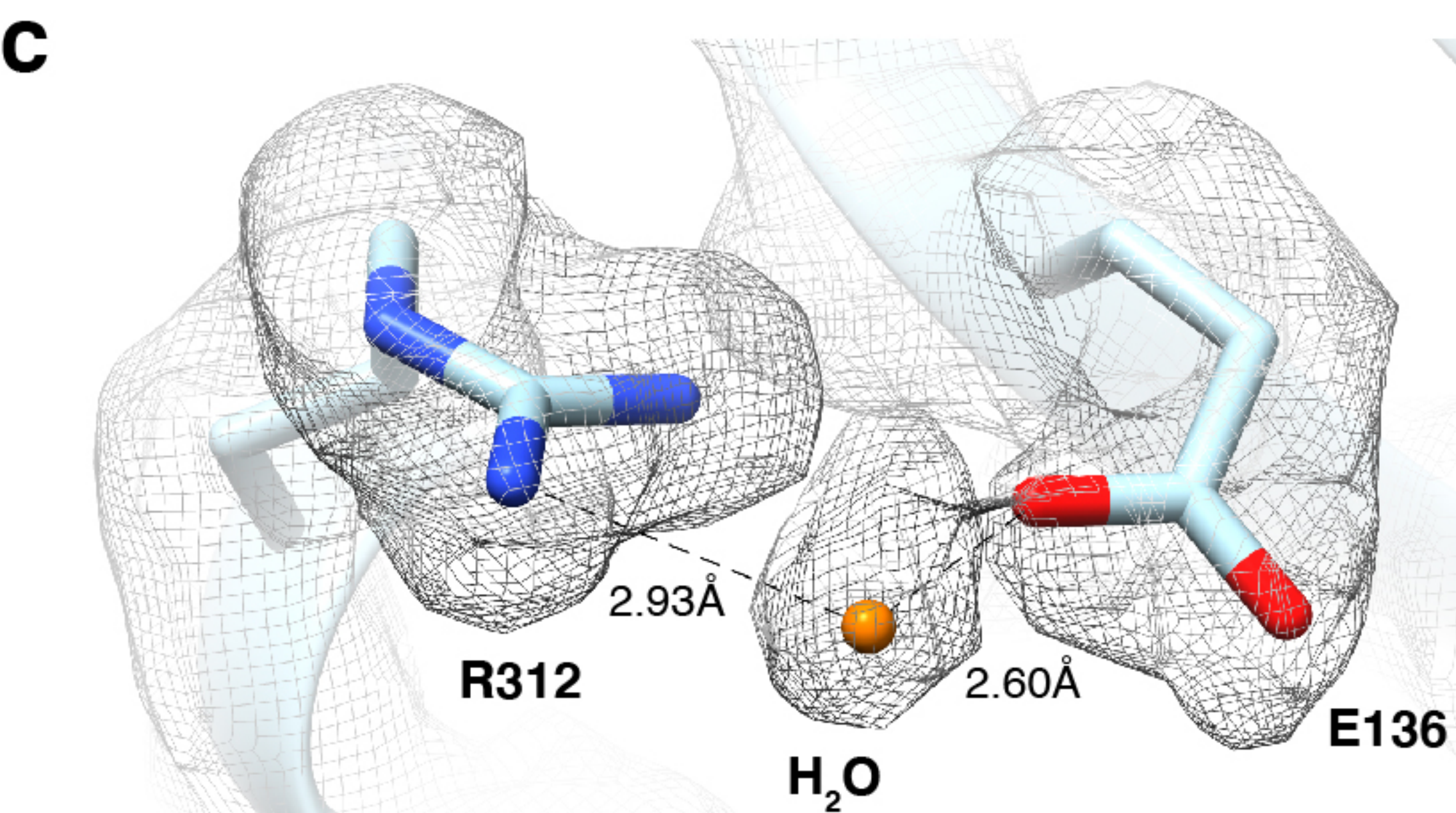
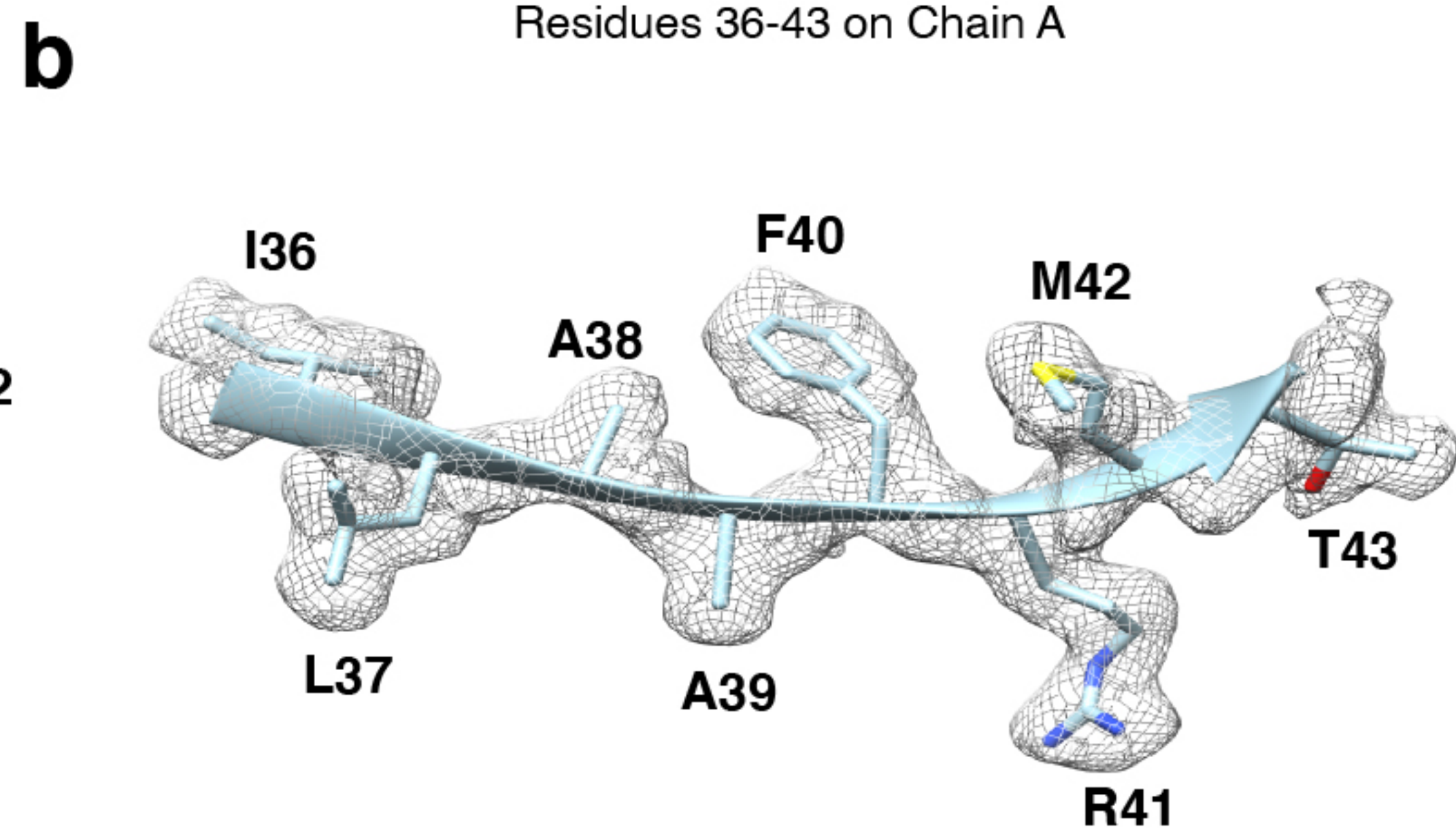
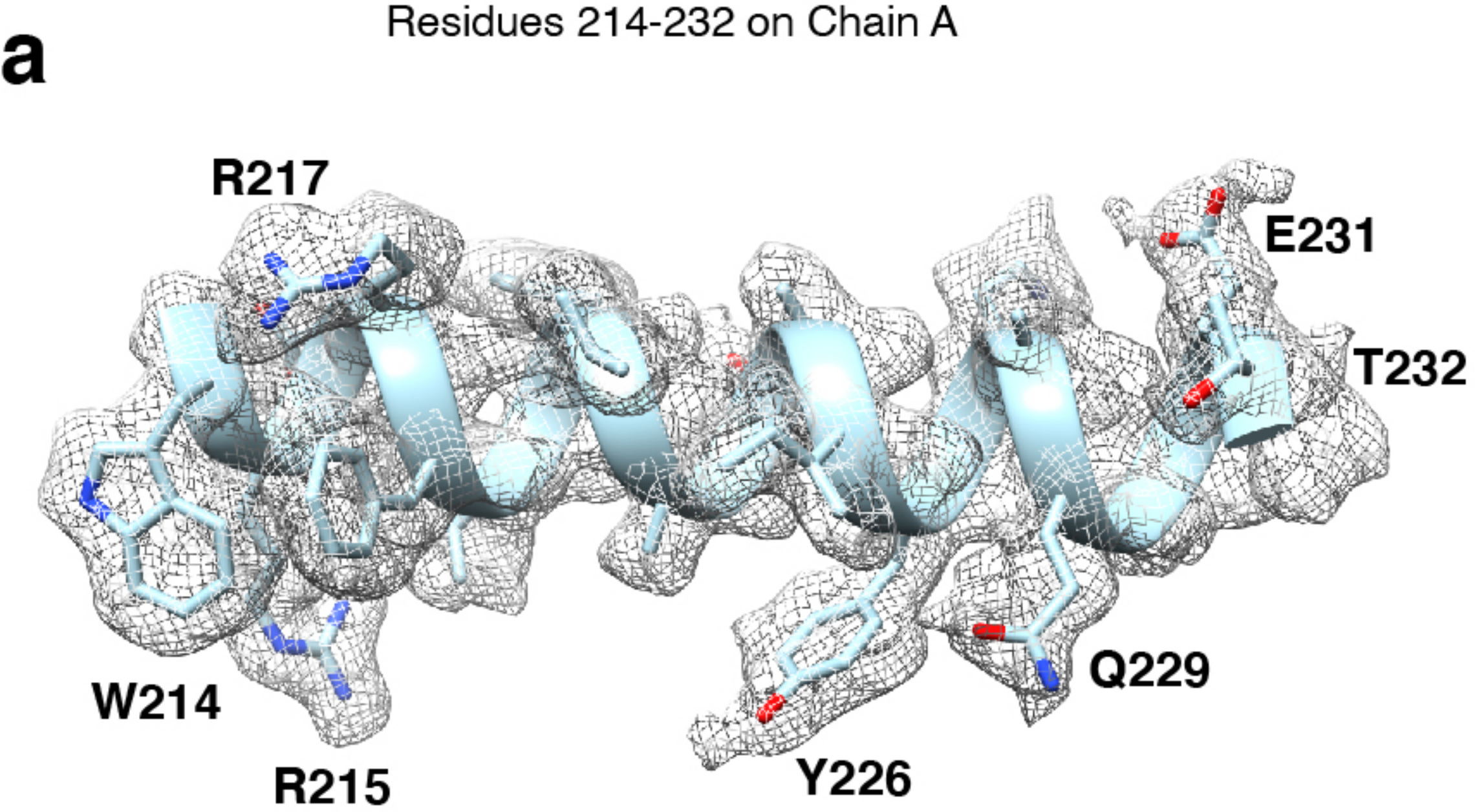


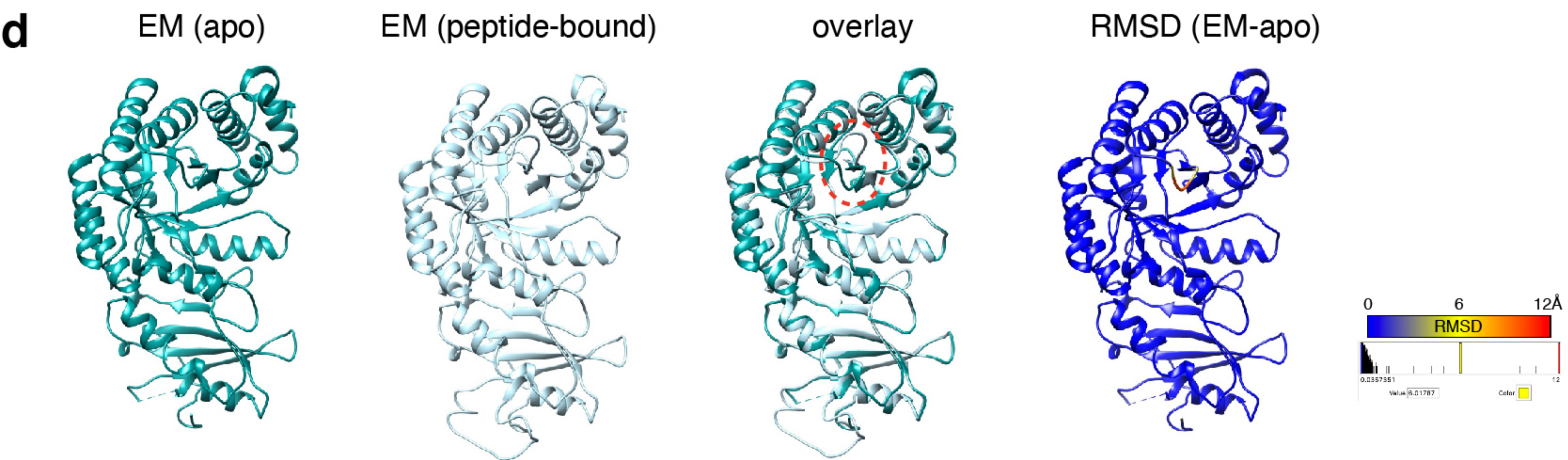
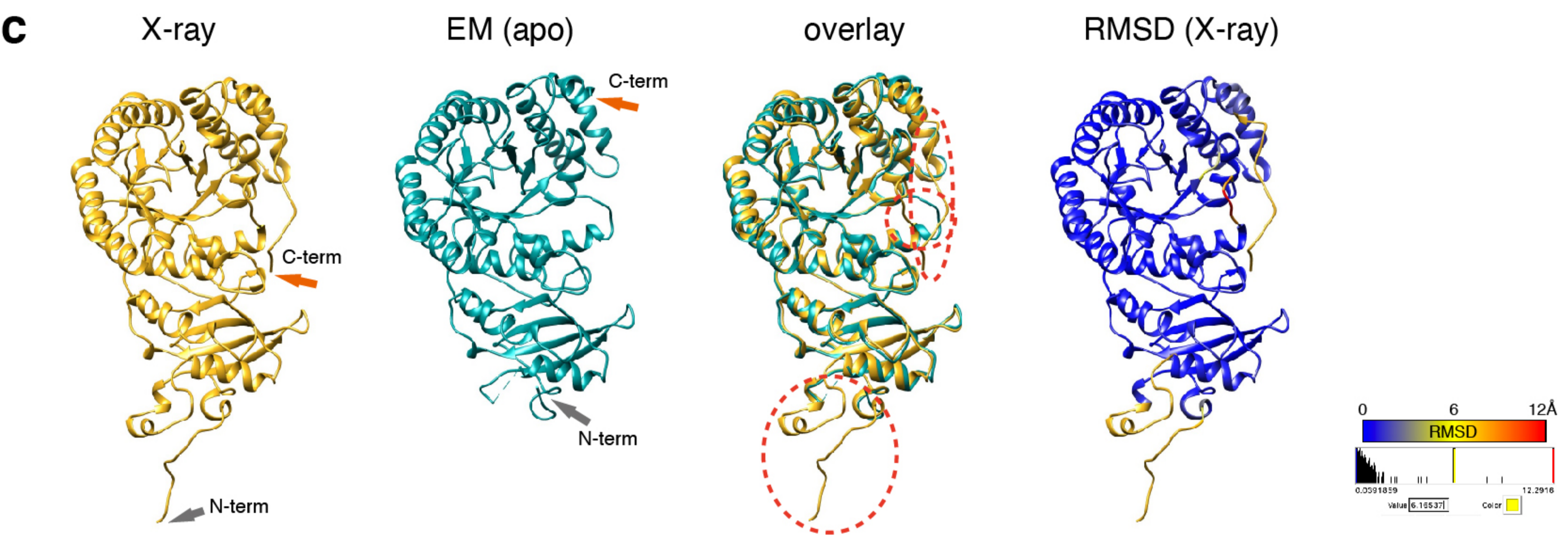
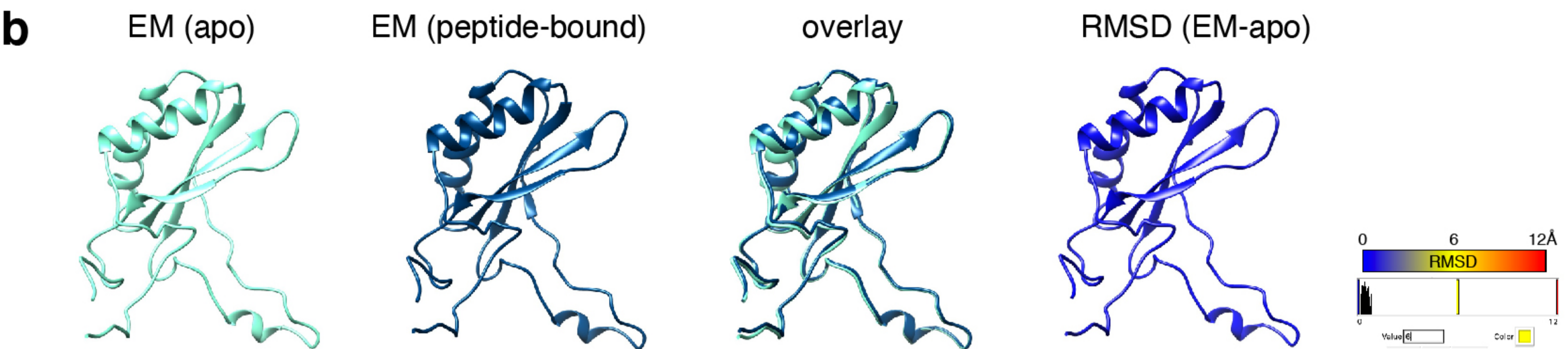
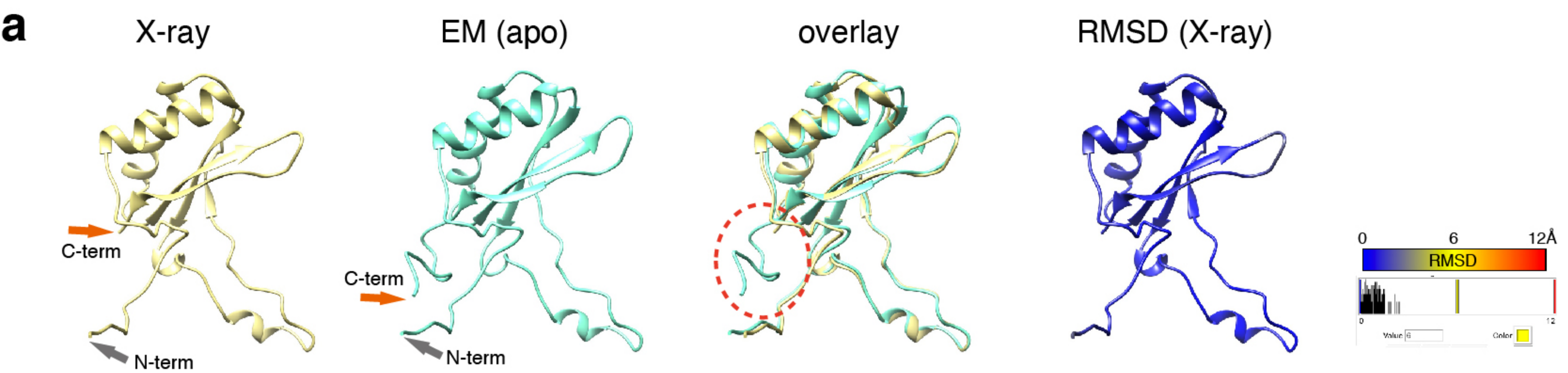
EPYC1₄₉₋₇₂ peptide-bound Rubisco
(2,500 micrographs)

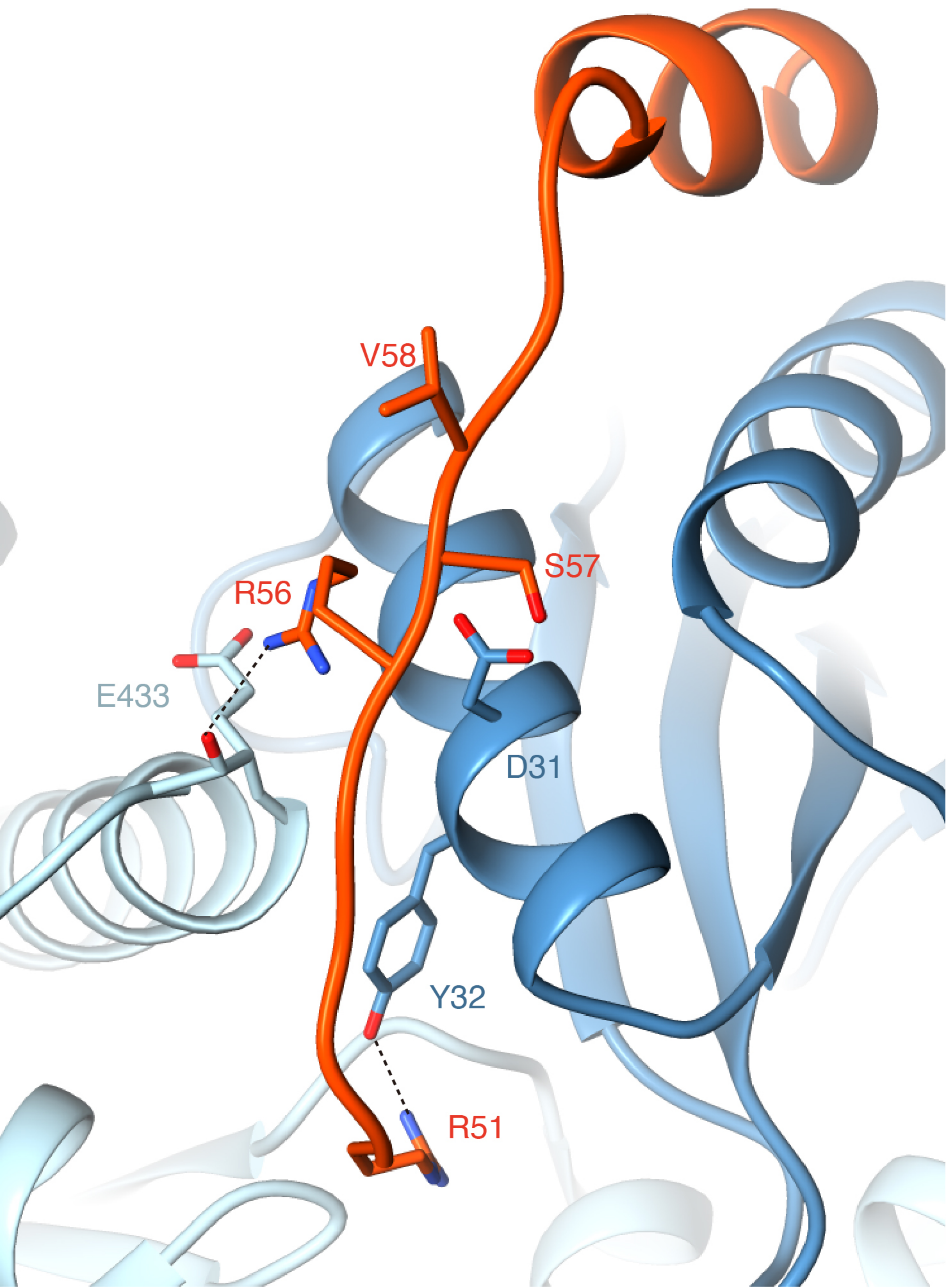


EPYC1₁₀₆₋₁₃₅ peptide-bound Rubisco
(13,727 micrographs)









V58

S57

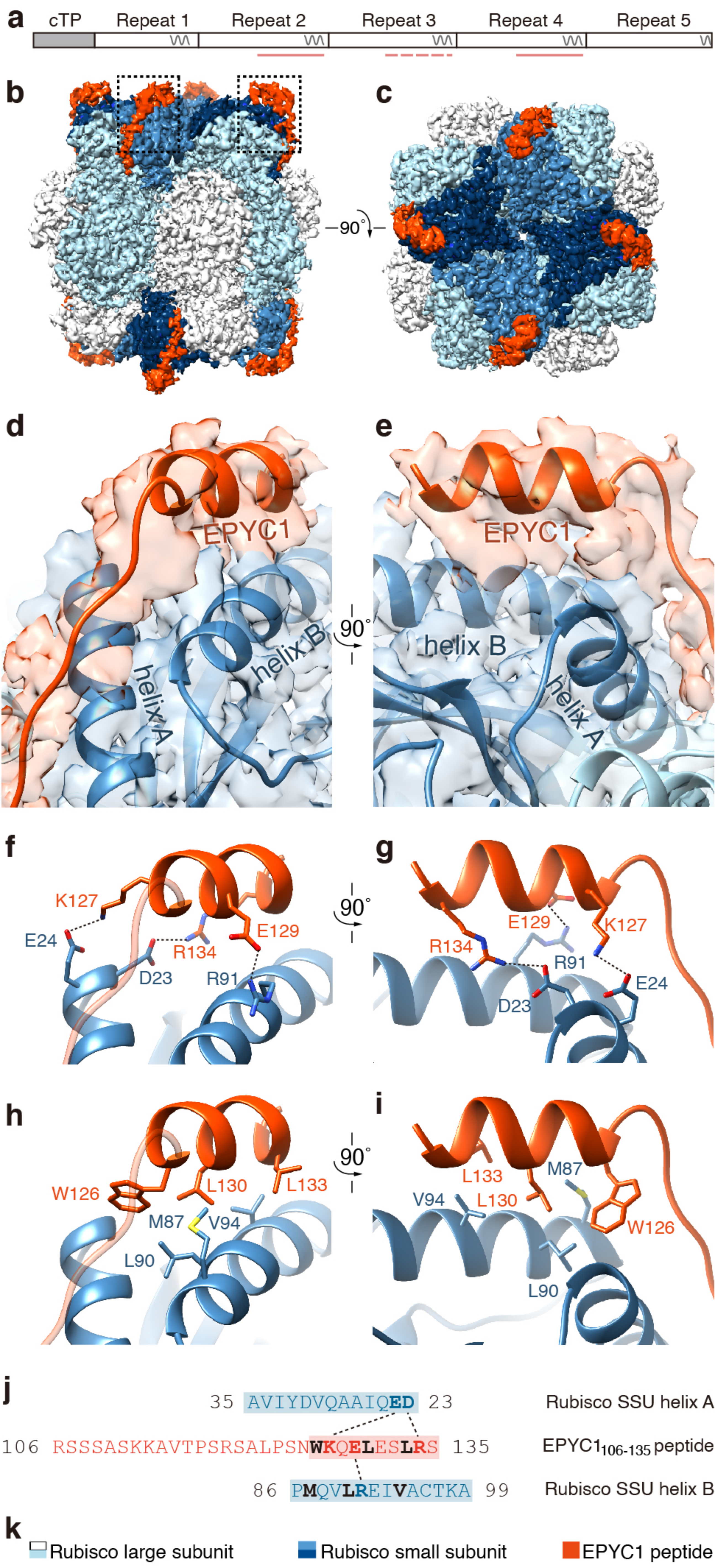
R56

E433

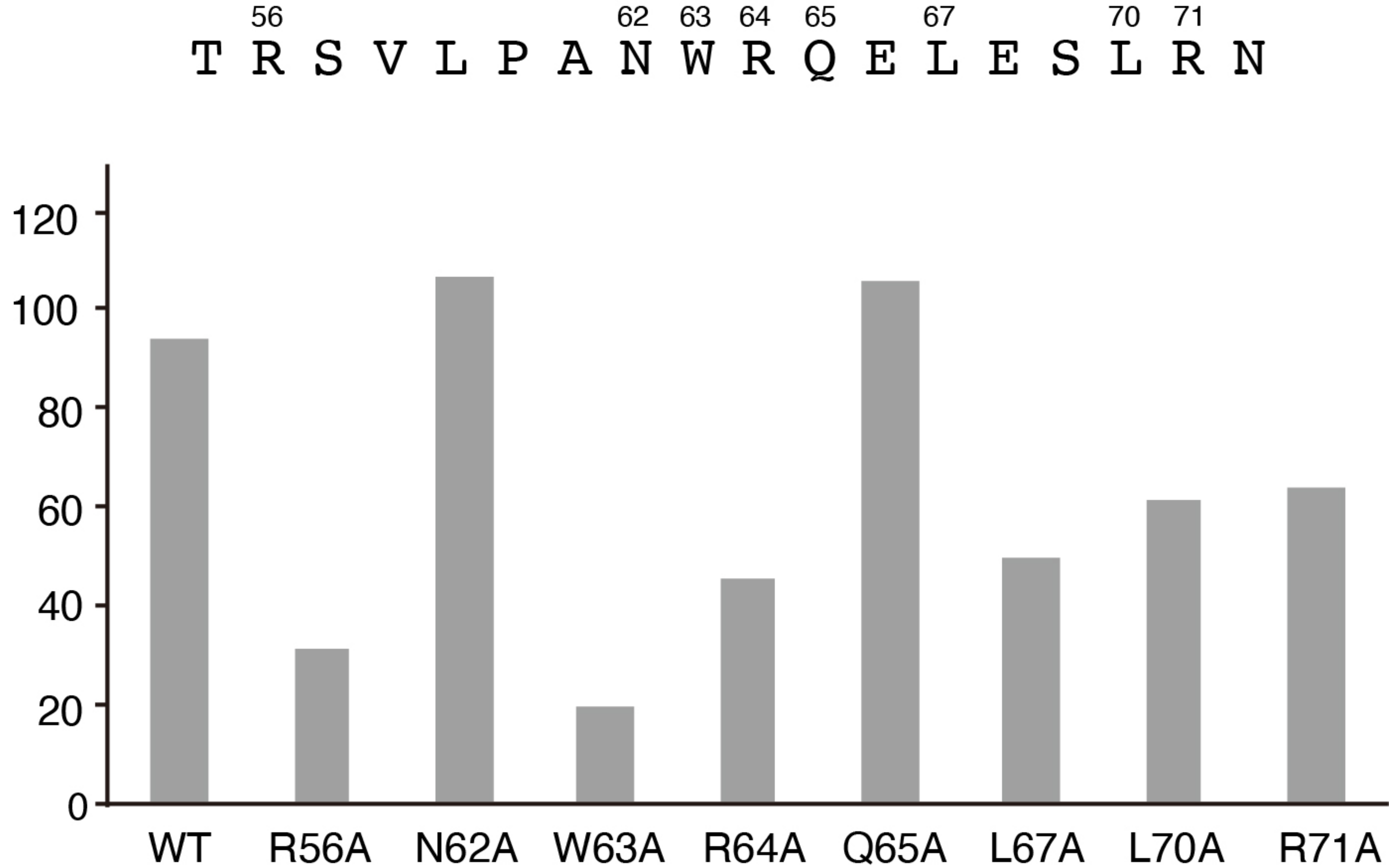
D31

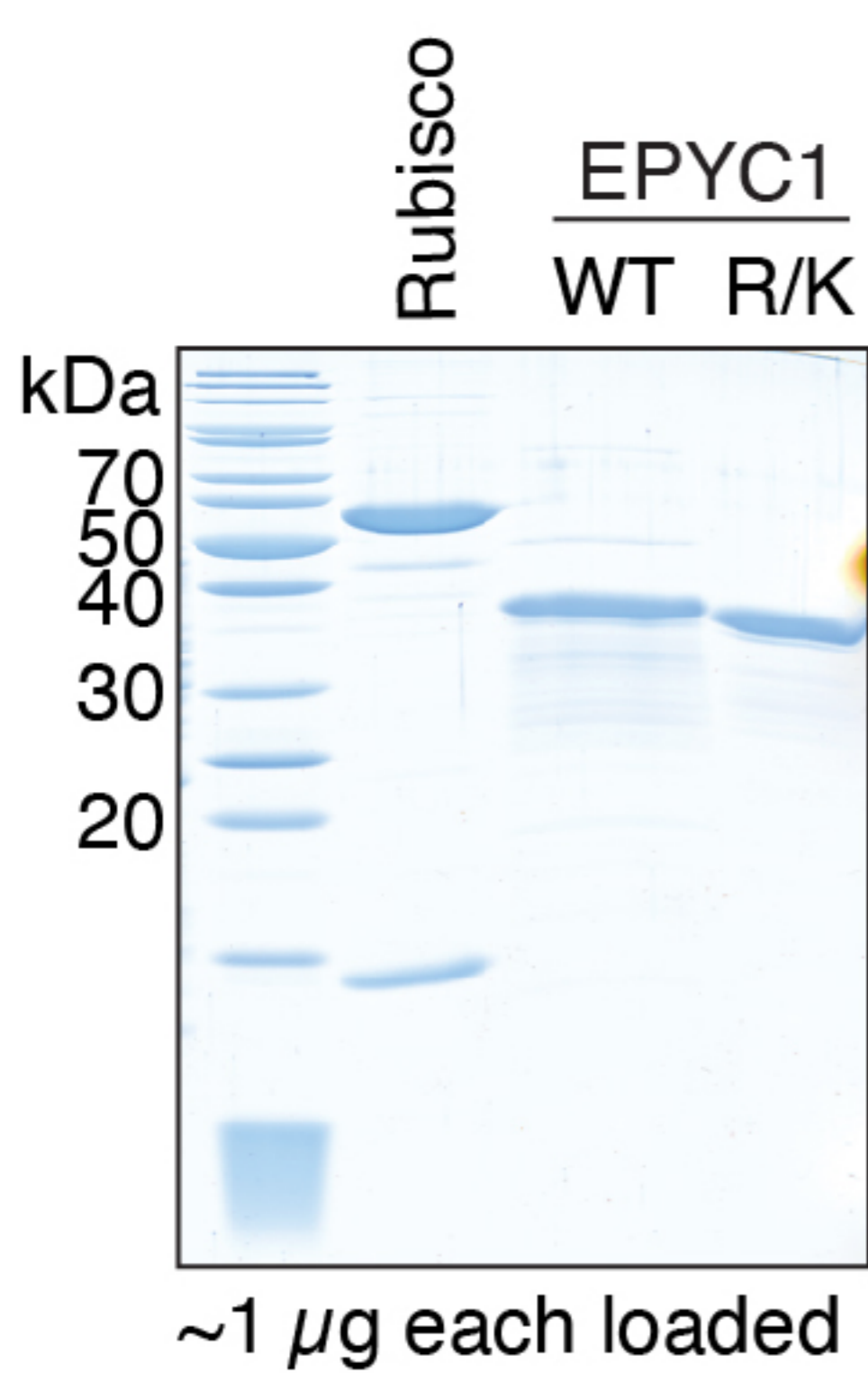
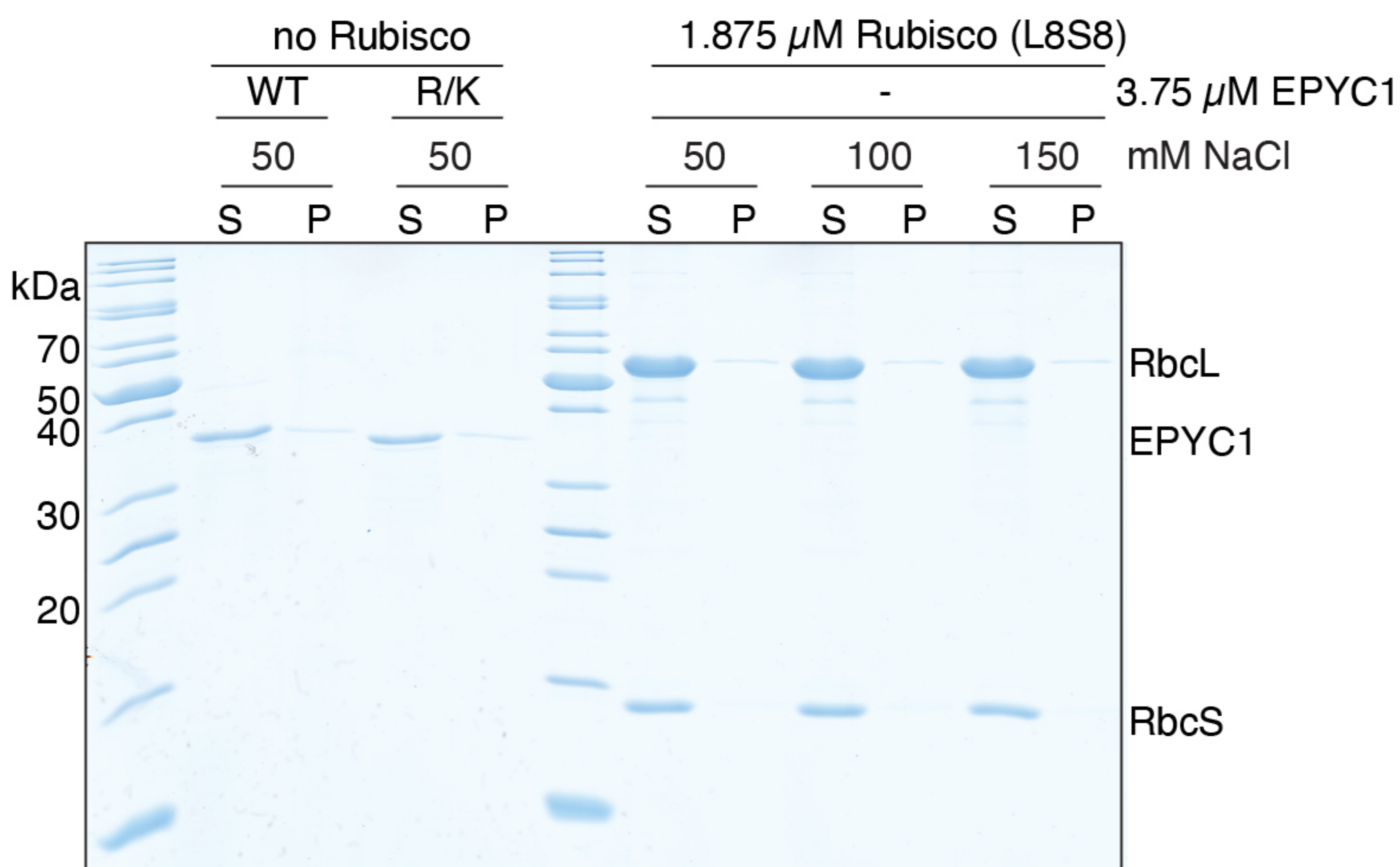
Y32

R51



Normalized binding to Rubisco (RU)



a**b****c**